

1 **Evaluating Intensity-Duration-Frequency (IDF) curves of satellite-based**
2 **precipitation datasets in Peninsular Malaysia**

3
4
5 Muhammad Noor¹, Tarmizi Ismail¹, Shamsuddin Shahid^{1,2*}, Md. Asaduzzaman³, Ashraf
6 Dewan⁴
7

8 ¹ School of Civil Engineering, Faculty of Engineering, Universiti Teknologi Malaysia
9 (UTM), Johor Bahru 81310, Malaysia;

10 mnkakar@gmail.com; tarmiziismail@utm.my; sshahid@utm.my
11

12 ² Centre for Coastal and Ocean Engineering (COEI), Universiti Teknologi Malaysia (UTM),
13 Johor Bahru 81310, Malaysia
14

15 ³ Department of Engineering & Design, Staffordshire University, Stoke-on-Trent ST4 2DE,
16 UK. Email: md.asaduzzaman@staffs.ac.uk
17

18 ⁴ Spatial Sciences Discipline, School of Earth and Planetary Sciences, Curtin University,
19 Perth, WA 6102, Australia. Email: a.dewan@curtin.edu.au
20

21 * Correspondence: hpsahar@utm.my
22
23
24
25
26
27
28
29
30

31 **Evaluating Intensity-Duration-Frequency (IDF) curves of Satellite-based**
32 **precipitation datasets in Peninsular Malaysia**

33
34 **Abstract**

35
36 In recent years the use of remotely sensed precipitation products in hydrological studies has
37 become increasingly common. The capability of the products in producing rainfall intensity-
38 duration-frequency (IDF) relationships, however, has not been examined in any great detail.
39 The performance of four remote-sensing-based gridded rainfall data processing algorithms
40 (GSMaP_NRT, GSMaP_GC, PERSIANN and TRMM_3B42V7) was evaluated to determine
41 the ability to generate reliable IDF curves. The work was undertaken in Peninsular Malaysia.
42 The best-fitted probability distribution functions (PDFs) of rainfall totals for different durations
43 were used to generate the IDF curves. The accuracy of the gridded IDF curves was evaluated
44 by comparing observed versus estimated IDF curves at 80 locations. The results revealed that
45 a generalized extreme value (GEV) distribution had the best fit to the rainfall intensity for
46 different durations at 62 % of the stations, and this was then used to develop the IDF curves. A
47 comparison of these remote sensing derived IDF curves with the observed IDF data revealed
48 that the GSMaP_GC product performed best. In general, the satellite-based precipitation
49 products tended to underestimate the IDF curves. The GSMaP_GC IDF curves were found to
50 be the least biased (8%–27%) compared to the TRMM_3B42V7 IDF curves (65%–67%). The
51 biases in rainfall intensity of different return periods for GSMaP_GC for all grid points were
52 estimated. These results can be used in designing hydraulic structures where gauged data are
53 unavailable.

54
55 **Keywords:** IDF curves, remote sensing precipitation products, probability distribution
56 function, ungauged location, bias correction

57
58

59 **1 Introduction**

60

61 The changing nature of the earth's climate is now widely recognised. One result of this climate
62 change is that the water holding capacity of the atmosphere is likely to increase (Trenberth,
63 2011). This has serious implications for the distribution of global precipitation (IPCC, 2014).
64 Changes in extreme rainfall events will occur due to increased evaporation and atmospheric
65 moisture content (Wang et al. 2014, Abbaspour et al., 2015; Pour et al., 2020a). Since rainfall
66 is the major element of the hydrological cycle, any additional change in its distribution and
67 volume may result in large scale flooding (Pour et al., 2014, Hajani et al., 2017; Pour et al.,
68 2020b), resulting in significant damage to infrastructures such as dams, stormwater drainage
69 systems (Shahid et al., 2017, Almazroui et al., 2019).

70 Global intensity-duration-frequency (IDF) curves are typically used to incorporate
71 hydrological information into water infrastructures design (Watt and Marsalek, 2013,
72 Koutsoyiannis et al., 1998, Şen, 2019). Such curves are based on the relationships between the
73 frequency, intensity and duration of rainfall data (Koutsoyiannis et al., 1998), and the use of
74 probability distribution functions (PDFs) of maximum rainfall depth (for a specific duration).
75 This enables a relationship to be defined between the properties of a specific rainfall episode
76 and the likelihood of rainfall totals (Chow et al., 1988). IDF curves can therefore be used to
77 estimate probable extreme rainfall totals over differing durations and intensities. A number of
78 studies have employed these IDF curves, utilising data from: a) in-situ rain-gauge (Willems,
79 2000; De Paola et al., 2014; Al-Amri and Subyani, 2017; Noor et al., 2018) and b) remote
80 sensing rainfall products (Endreny and Imbeah, 2009; Liew et al., 2014; Marra et al., 2017;
81 Ombadi et al., 2018; Courty et al., 2019); both at local and global scales.

82 Traditionally ground-based rain gauge data has been used to construct IDF curves.
83 Unfortunately a lack of consistent rainfall records at high temporal resolutions (hourly or sub-
84 hourly) and a spatial sparseness of weather stations in many locations, are major barriers to the
85 successful generation of IDF curves, particularly in countries where data is scarce (Nashwan
86 and Shahid, 2019a, Prein and Gobiet, 2017, Nashwan et al., 2018). As the spatial nature of IDF
87 curves vary widely due to variations in the pattern of rainfall intensity and duration (Kidd et
88 al., 2017, Sorooshian et al., 2011), it is common to use data from nearby recording stations to
89 generate IDFs. This, however, may not be an ideal solution when used in the design of water
90 infrastructure as it has been found that the accuracy of IDF curves tends to decrease
91 significantly with distance from rain gauge locations (Marra et al., 2017). To overcome the
92 difficulties associated with sparse observational records, alternative data source is suggested to

93 tackle engineering challenges (Courty et al., 2019), induced by climate warming (Liew et al.,
94 2014).

95

96 A range of global, gridded precipitation products are now available which may be categorized
97 as gauge-based (Herrera et al., 2012; Schiemann et al., 2010; Yatagai et al., 2009; Faiz et al.,
98 2018), remote sensing-based (Nashwan and Shahid, 2019b; Huang et al., 2018; Palomino-
99 Ángel et al., 2019; Almazroui and Saeed, 2020), reanalysis-based (Belo-Pereira et al., 2011;
100 Yao et al., 2020), as well as a combination of the above three (Alijanian et al., 2017; Laiti et
101 al., 2018). Because their spatial and temporal (hourly or sub-hourly) resolution is reasonably
102 high, remotely sensed data products are particularly useful in developing IDF curves for hydro-
103 climatic studies conducted at ungauged and data-sparse locations (Yang et al., 2014, Prakash
104 et al., 2015, Belo-Pereira et al., 2011, Herrera et al., 2012, Schiemann et al., 2010, Yatagai et
105 al., 2009, Nashwan and Shahid, 2019b). Furthermore, gridded precipitation data can assimilate
106 the variability and dynamics of extreme rainfall events at ungauged locations which cannot be
107 captured by rain gauges, and can thus help in overcoming issues related to the interpolation of
108 point data (Chen et al., 2013, Marra et al., 2016, Panziera et al., 2016). The use of remotely
109 sensed precipitation products in hydrological studies is, therefore, an area of increasing
110 research focus.

111

112 Despite extensive use of gridded precipitation products obtained from satellite observation,
113 such as stream flow simulation (Kumar and Lakshmi, 2018), flood modelling (Yuan et al.,
114 2019, Nashwan et al., 2019), aridity assessment (Hasan et al., 2019), statistical structure of
115 rainfall behaviour (Dewan et al., 2019), drought observation (Jiang et al., 2017, Yang et al.,
116 2018), only a handful works have been conducted to date in developing IDF curves in different
117 regions. This includes areas of the United States (Wright et al., 2013; Ombadi et al., 2018),
118 eastern Mediterranean region (Marra et al., 2017), Netherlands (Overeem et al., 2009) and
119 Ghana (Endreny and Imbeah, 2009) and nine different cities of the world (Courty et al., 2019).
120 The studies that have used gridded precipitation products, either from satellite or reanalysis,
121 have shown immense potential, particularly in locations where precipitation data is scarce. For
122 example, Courty et al. (2019) developed a universal IDF formula at the global scale using
123 ERA5 reanalysis data. (Ombadi et al., 2018) developed IDF curves over the USA using
124 PERSIANN-CDR data. Marra et al. (2017) developed IDF curves for East Mediterranean
125 regions using radar and satellite (CMORPH) rainfall. Endreny and Imbeah (2009) used TRMM

126 and observed rainfall data to develop IDF curves in Ghana. These studies suggest that a
127 potential issue could be the reliability of the satellite-derived rainfall products as this differs
128 from place to place, depending on the calculation processes and specific weather conditions
129 (Serrat-Capdevila et al., 2016, Tan and Duan, 2017, Chen and Li, 2016). As a result, IDF curves
130 developed from gridded rainfall data tend to deviate from curves developed from the observed
131 rainfall data (Peleg et al., 2018). An exact match between IDF curves is not possible when the
132 curves have been generated using two different datasets – (i) gridded, precipitation-based
133 curves, and (ii) gauged-based IDF curves (Marra et al., 2017). Endreny and Imbeah (2009) also
134 suggested that the combined use of the satellite and observed data could provide useful insights
135 for generating the IDF curves. It is essential to find the best remote sensing data product in
136 order to generate bias-free or least biased IDF curves, and to subsequently correct the bias of
137 remote sensing based IDF curves prior to use in any hydraulic design work.

138

139 The IDF curves at sub-daily scale are of prime importance in designing hydraulic structures
140 (Lima et al., 2018). The urban catchments are sensitive to shorter rainfall events and thus
141 requires a drainage system designed based on sub-daily IDF curves (Courty et al., 2019). The
142 IDF curves at sub-daily temporal resolution are particularly important for tropical regions
143 where intense short-duration rainfall is very common (Tien and Dutto, 2018). The aim of this
144 current work is to assess the ability of remotely sensed precipitation data to generate sub-daily
145 IDF curves. Four remote sensing rainfall products, namely Global Satellite Mapping of
146 Precipitation - Gauge Calibrated (GSMaP), Global Satellite Mapping of Precipitation - Near
147 Real-Time (GSMaP_NRT), Precipitation Estimation from Remotely Sensed Information using
148 Artificial Neural Networks (PERSIANN), and Tropical Rainfall Measuring Mission (TRMM),
149 are used to generate sub-daily IDF curves in countries where data is difficult to obtain.
150 Although several remote sensing data products are available for use in hydrological studies,
151 the temporal resolution and short period of availability have restricted their application. The
152 hourly rainfall data for longer periods were available only for GSMaP_GC, GSMaP_NRT,
153 PERSIANN and TRMM, and so only the performance of these products in developing of IDF
154 curve was assessed in this study.

155

156

157 **2 Materials and methods**

158 *2.1 Study area*

159

160 The study area is located in Peninsular Malaysia between latitudes 1.20° N and 6.80° N, and
161 longitudes 100.10° E and 104.20° E (Figure 1). The area annually records 2000–4000 mm of
162 rain from 150-200 wet days due to the tropical, humid climate (Nashwan et al., 2018, Noor et
163 al., 2019). Monsoon winds, complex land-sea interactions and mountainous topography control
164 the spatial variation of rainfall in the region (Pour et al., 2020c). Extreme rainfall events usually
165 occur during the northeast monsoon (November to March), although these rainfall events can
166 also occur during the inter-monsoon period (September–October and March–April),
167 particularly in the west of the Peninsula (Mayowa et al., 2015; Khan et al., 2019). The mean
168 annual temperature in the study area ranges from 21° C to 32°C.

169

170

171

172

173

174

175

176

177

178

179

180

181

182

183

184

185

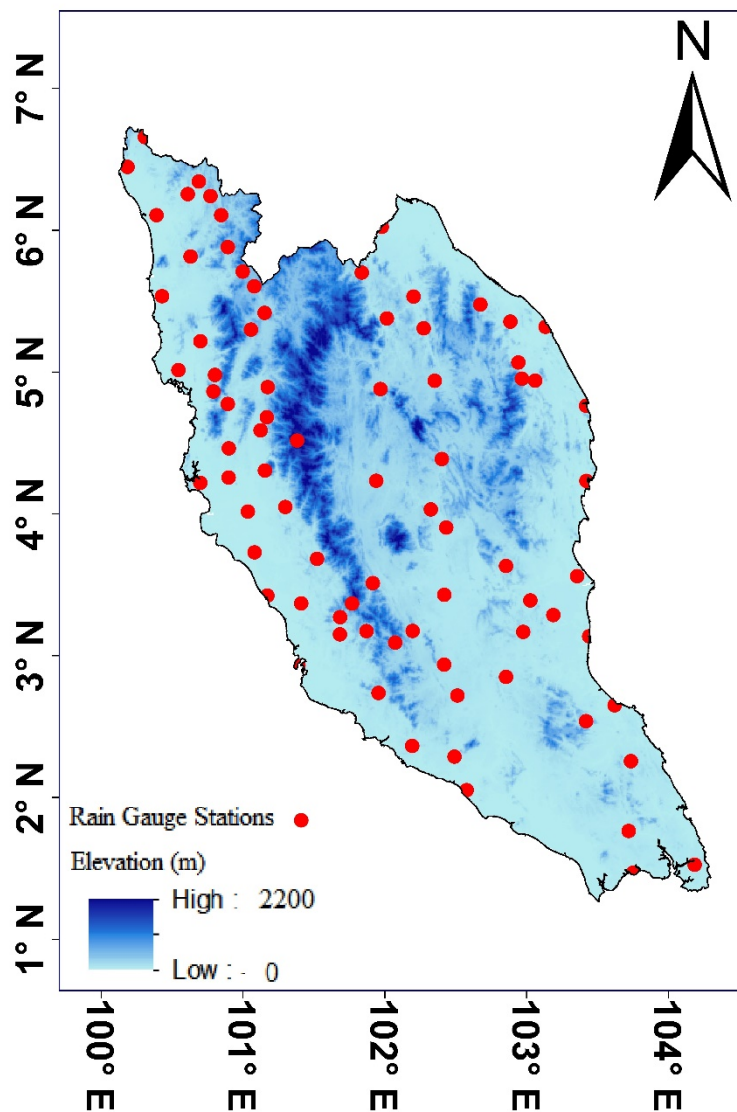
186

187

188

189

190



191 **Figure 1** Geographical boundary and topography of Peninsular Malaysia. Rain gauge stations
192 used in this work are shown

193

194 *2.2 Observed rainfall data*

195

196 Hourly rainfall data from the 80 rain gauge stations distributed across the Peninsula were
197 obtained from the Department of Irrigation and Drainage (DID), Malaysia. Locations of these
198 stations are shown in Figure 1. A common period of data for observed rainfall and satellite-
199 based products (2000-2018) was used.

200

201 DID uses a standardised procedure for the measurement and archiving of rainfall data. In
202 previous hydro-climatic studies conducted in this area, the quality of the DID rainfall data was
203 found to be fit-for-purpose (Mayowa et al., 2019), however as part of the normal due diligence
204 process, the quality of the rainfall data to be used in the current study was evaluated prior to
205 processing using both subjective and objective evaluation methods. DID has 199 rain gauges
206 available to record rainfall in Peninsular Malaysia. Data from 80 stations missing less than 1%
207 of the hourly data for the 2000 to 2018 period were selected. Checks included looking for an
208 absence of negative values, presence of hourly rainfall figures showing more than 50 mm, and
209 one-day cumulative rainfall figures of more than 200 mm. Hourly, daily and monthly rainfall
210 time series and histogram plots were prepared to find any irregularity in the dataset (Ahmed et
211 al., 2019). Hourly and daily average values over a day and a year respectively were prepared
212 to evaluate the consistency of the data. Data quality was also assessed using sequential student
213 t-tests. All the rainfall data was deemed to be of adequate quality for the work and no
214 abnormalities in the plots was noted. No significant differences among the different subsets of
215 data was noted using the t-test.

216

217 *2.2.2 Remote sensing precipitation data*

218

219 Four remotely sensed precipitation data products were acquired and evaluated in the present
220 study (Table 1). The GSMaP precipitation product is collected and compiled by Core Research
221 for Evolutional Science and Technology (CREST) of the Japan Science and Technology
222 Agency (JSTA) in collaboration with the Japan Aerospace Exploration Agency (JAXA)
223 Precipitation Measuring Mission (PMM) Science Team (Okamoto et al., 2005, Ushio et al.,
224 2009). It comprises two products - (i) GSMaP_NRT, developed by integrating global

225 precipitation rates extracted from passive microwave radiometers and cloud moving vectors
 226 derived from infrared images, and (ii) GSMaP_GC, which is an adjusted product of
 227 GSMaP_NRT using the NOAA Climate Prediction Center (CPC) precipitation data (Nashwan
 228 and Shahid, 2019b). PERSIANN is precipitation estimated from geostationary satellite-based
 229 infrared brightness temperature using a neural network function (Nguyen et al., 2018). It is
 230 produced by the Center for Hydrometeorology and Remote Sensing (CHRS) at the University
 231 of California, Irvine (UCI). Tropical Rainfall Measuring Mission (TRMM) data is a joint
 232 mission between JAXA and NASA (Huffman, 2016). In this study, 3-hour real time TRMM
 233 multi-satellite precipitation analysis information (TRMM_3B42V7) (Mission, 2011) is used.
 234

235 **Table 1** Remote sensing precipitation datasets used in this study

Data Set	Temp Resoluti on	Period	Pixel size	Source
GSMaP_NRT	1-hour	2000—till	0.1×0.1	https://sharaku.eorc.jaxa.jp/GSMaP/index.htm
GSMaP_GC	1-hour	2000—till	0.1×0.1	https://sharaku.eorc.jaxa.jp/GSMaP/index.htm
PERSIANN	3-hour	2000—till	0.25×0.25	https://chrsdata.eng.uci.edu/
TRMM_3B42V7	3-hour	1997—2019	0.25×0.25	https://pmm.nasa.gov/data-access/downloads/trmm

236

237

238 3 Methodology

239

240 3.1 General IDF relationship for different distributions

241 The intensity-duration-frequency (IDF) relationship is a popular method that relates rainfall
 242 intensity with its duration and annual frequency. For a given duration d , return period T and
 243 the maximum intensity $i(d, T)$ of rainfall at a specific location, the general form of the
 244 intensity-duration-frequency (IDF) curve (Koutsoyiannis et al., 1998) can be formulated as:

$$245 \quad i(d, T) = a(d, T) \cdot (d + \theta)^{-\eta}, \quad (1)$$

246 where $a(d, T)$ and $i(d, T)$ are functions of d and T , θ and η are parameters with $\theta > 0$ and
 247 $1 < \eta < 0$. Koutsoyiannis et al. (1998) established the relationship between the cumulative
 248 distribution function (CDF) of the maximum intensity and the return period T given as:

$$249 \quad a(d, T) = F_Y(y_T) = 1 - \frac{1}{T}. \quad (2)$$

250 The IDF relationship (Koutsoyiannis et al., 1998) between the maximum amounts of rainfall
251 with distribution function $F_Y(\cdot)$ with T for d is, therefore, presented as:

$$252 \quad y_T = a(d, T) = F_Y^{-1}(1 - 1/T). \quad (3)$$

253

254 In this study, we consider four widely used probability distributions to fit IDF curves and
255 evaluate the individual performances. These are Exponential, Generalised Pareto (GP),
256 Gumbel and Generalized Extreme Value (GEV). The exponential distribution is a fundamental
257 distribution for establishing several other distributions. The exponential distribution function
258 is broadly applied in hydrological studies (Kjeldsen et al., 2000). This distribution has
259 applicability in such things as the frequency analysis of rainfall amount and extreme events
260 (Zhu et al., 2019). The PDF of the exponential random variable is given by:

$$261 \quad F(y) = \begin{cases} 1 - \exp\left(-\frac{y}{\lambda} + \psi\right), & x \geq 0 \\ 0, & otherwise \end{cases} \quad (4)$$

262 where λ and ψ are the scale and location parameters respectively. The IDF relationship for the
263 exponential distribution (Koutsoyiannis et al., 1998) can be expressed as:

$$264 \quad y_T \equiv a(T) = \lambda(\psi + \ln T). \quad (5)$$

265 Pikands (1975) suggested the Generalized Pareto (GP) distribution, which has been
266 applied in the various fields. GP distribution plays a significant role in modelling of extreme
267 events e.g., the analysis of the highest annual flood values, the precipitation data analysis, in
268 the analysis of flood frequency, etc. The PDF of generalized pareto distribution is expressed
269 as:

$$270 \quad F(y) = 1 - \left[1 + k\left(\frac{y}{\lambda} - \psi\right)\right]^{-\frac{1}{k}}, \quad y \geq \lambda\psi \quad (6)$$

271 where k is the shape parameter. For the GP distribution, the IDF relationship (Koutsoyiannis et
272 al., 1998) is obtained as:

$$273 \quad y_T \equiv a(T) = \lambda \left(\psi + \frac{T-1}{k}\right). \quad (7)$$

274 Gumbel distribution or Extreme Value Type I (EV1) distribution is often used in the
275 frequency analysis of hydrological extremes e.g., floods, storms, wind speed, droughts, etc.
276 (Yue and Wang, 2004; Hong et al., 2013). The PDF of Gumbel distribution can be given as:

277 $F(y) = \exp \left(- \exp \left(\frac{-y}{\lambda} + \psi \right) \right)$ (8)

278 The IDF relationship for Gumbel distribution (Koutsoyiannis et al., 1998) can be given by

279 $y_T \equiv a(T) = \lambda \left(\psi - \ln \left[-\ln \left(1 - \frac{1}{T} \right) \right] \right)$. (9)

280 The Generalized Extreme Value (GEV) distribution (developed within the extreme
 281 value theory) is a family of continuous probability distributions. The GEV distribution
 282 originated from the extreme value axiom and is the limit distribution of normalized maxima of
 283 an independent and identically distributed random variable. The PDF of the GEV is represented
 284 as (Jenkinson, 1955),

285 $F(y) = \exp \left(- \left[1 + k \left(\frac{y}{\lambda} - \psi \right) \right]^{-1/k} \right), \quad y \geq \lambda(\psi - 1/k)$ (10)

286 Koutsoyiannis et al. (1998) established the IDF relationship for the GEV distribution can be
 287 given as:

288 $y_T \equiv a(T) = \lambda \left(\psi + \frac{[-\ln(1-\frac{1}{T})]^{-k} - 1}{k} \right)$. (11)

289

290 *3.2 Estimation of Parameters and Fitting IDF Curve*

291 The Maximum Likelihood Estimation (MLE), Generalized Maximum Likelihood Estimation
 292 (GMLE), Bayesian and L-moments are commonly used methods for fitting PDFs for annual
 293 extreme rainfall time series data (Martins & Stedinger, 2000). In this study, performance of all
 294 the four methods were compared to find the best parameter estimation method. Goodness of fit
 295 test was used for the selection of best parameter estimation method. Several goodness of fit
 296 tests are available in practice, but there is no general criteria for selection of suitable goodness
 297 of fit test (Rahman et al., 2013). However, the log likelihood approach developed by R.A Fisher
 298 (Fisher, 1912) is most widely used for performance assessment of PDF parameter estimation
 299 method (Fienberg, 1997, Zhu et al., 2018, Bierman et al., 1989, Poudel and Cao, 2013).

300 The likelihood is the joint density of n independent observations, $y = (y_1 \dots y_n)'$ which can
 301 be expressed as,

302 $L(\theta) = f(\mathbf{y}|\theta) = \prod_{i=1}^n f(y_i | \theta)$, (12)

303 where $f(y|\theta)$ is the PDF and θ is the unknown parameter (Hilbe & Robinson, 2013). Often,
 304 natural logarithm of the likelihood function $L(\theta)$ is called the log-likelihood function ($LL(\theta)$),

305 which is used to estimate parameters (instead of the likelihood function) due to mathematical
 306 tractability. Due to the monotonicity property, the estimates from the log-likelihood function
 307 $LL(\theta)$ also gives the same estimates by retaining all properties (Hilbe & Robinson, 2013). The
 308 $LL(\theta)$ is defined as

$$309 \quad LL(\theta) = \ln L(\theta) = \sum_{i=1}^n \log f(y_i | \theta). \quad (13)$$

310 For ease of computation, the negative logarithm of the likelihood estimates or the negative log
 311 likelihood is commonly practiced (Bosman and Thierens, 2000).

312 The GMLE estimates parameters in a similar manner to that used in the MLE method (Martins
 313 & Stedinger, 2000). Additional conditions eliminate the set of potential invalid values on some
 314 parameters while estimating the parameter of interest. This is done by setting initial
 315 distributions for those parameters (Martins & Stedinger, 2000). The GMLE involves solving
 316 the following optimization problem,

$$317 \quad \begin{aligned} & \max_{\theta} L_n(x; \theta) \\ & \beta \sim \text{gamma}(u, v) \end{aligned} \quad (14)$$

318 where θ is the parameter of interest and β is the other parameter which follows a gamma prior
 319 distribution. The GMLE method is, therefore, analogous to the Bayes estimation method as it
 320 is equivalent to maximizing a posterior distribution. Since the posterior form is unknown, in
 321 general, numerical techniques like Markov chain Monte Carlo (MCMC) is applied to calculate
 322 parameters.

323

324 Bayesian method of parameter estimation involves specifying a prior probability density
 325 function, say $\pi(\theta)$ (Reis & Stedinger, 2005). After the prior has been specified, the posterior
 326 distribution of θ is computed, and from this inferences can be made. Using Bayes Theorem,
 327 the conditional density of θ given data y_1, y_2, \dots, y_n is written as

$$328 \quad \pi(\theta | y_1, y_2, \dots, y_n) = \frac{f(y_1, y_2, \dots, y_n | \theta) \pi(\theta)}{f(y_1, y_2, \dots, y_n)} = \frac{[\prod_i f(y_i | \theta)] \pi(\theta)}{\int_{\Omega} [\prod_i f(y_i | \theta)] \pi(\theta) d\theta}, \quad (15)$$

329 where Ω is the parameter space. Re-writing $\prod_i f(y_i | \theta)$ as the likelihood function, $L(y_i | \theta)$,
 330 we get

$$331 \quad \pi(\theta | y_1, y_2, \dots, y_n) = \frac{L(y_i | \theta) \pi(\theta)}{\int_{\Omega} L(y_i | \theta) \pi(\theta) d\theta}. \quad (16)$$

332 The posterior distribution is then maximized for the parameter values θ (Reis & Stedinger,
333 2005).

334

335 Hosking (1986, 1990) proposed the L-moments method which is frequently used for the
336 characterization of data, characterizaion of PDFs, testing of PDF hypotheses and parameter
337 estimation of PDFs. For a real valued ordered random variate Y of n samples, $y_{1:n} \leq y_{2:n} \leq$
338 $\dots \leq y_{n:n}$ for cdf $F(y)$ and quantile function $y(F)$, the r -th L-moment of Y can be described as
339 a linear function of the expected order statistics and can be represented as (Hosking, 1990)

$$340 \lambda_r = \frac{1}{r} \sum_{k=0}^{r-1} (-1)^k \binom{r-1}{k} EY_{r-k:r}, \quad r = 1, 2, 3 \dots \quad (17)$$

341 The letter 'L' in 'L-moments' reveals the fact that r -th L-moment λ_r is a linear function of the
342 expected order statistics. Furthermore, based on the observed sample the natural estimate of the
343 L-moment λ_r is the L-statistics. The probable value of order statistics can be represented as:

$$344 E(Y_{j:r}) = \frac{r!}{(j-1)!(r-j)!} \int y[F(y)]^{j-1} [1 - F(y)]^{r-j} dF(y). \quad (18)$$

345 The first four L-moments are derived as (Hosking, 2006):

$$346 \lambda_1 = E(Y) = \int_0^1 y(F) dF, \quad (19)$$

$$347 \lambda_2 = \frac{1}{2} E(Y_{2:2} - Y_{1:2}) = \int_0^1 y(F) (2F - 1) dF, \quad (20)$$

$$348 \lambda_3 = \frac{1}{3} E(Y_{3:3} - 2Y_{2:3} + Y_{1:3}) = \int_0^1 y(F) (6F^2 - 6F + 1) dF, \quad (21)$$

$$349 \lambda_4 = \frac{1}{4} E(Y_{4:4} - 3Y_{3:4} + 3Y_{2:4} - Y_{1:4}) = \int_0^1 y(F) (20F^3 - 3F^2 + 12F - 1) dF. \quad (22)$$

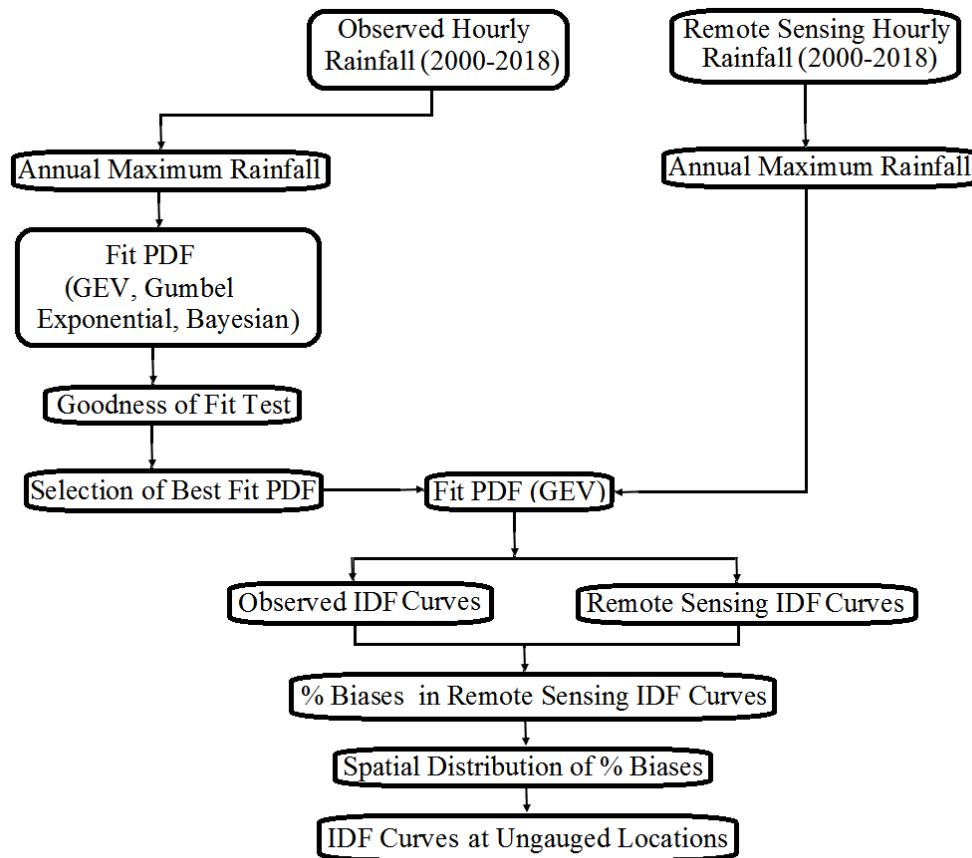
350

351 3.3 Development of IDF Curves

352

353 The process used for the development of the IDF curves is shown in Figure 2. The parameters
354 of best-fitted PDF are used to generate observed IDF curves, using hourly rainfall observations
355 and remotely sensed-based rainfall IDF curves at 80 stations. They are developed by fitting the
356 PDF to annual precipitation maximum data e.g. annual maximum of daily one-, two-, three-,
357 or more hour rainfall amount. The parameter of the fitted PDFs is then applied to calculate the
358 return period of maximum rainfall depth for each duration. The return periods of the rainfall
359 intensities of corresponding durations are then plotted to prepare the IDF curves. In the present

360 study, IDF curves are constructed for 2-, 5-, 10-, 2-5, 50- and 100-year return periods and 1-,
 361 3-, 6-, 12-, 24-, 48- and 72-hour rainfall durations.



362
 363 **Figure 2** Flowchart showing the development of IDF curves

364
 365 *3.4 Performance Assessment*

366
 367 Two approaches can be used for comparing gridded rainfall data with in-situ rainfall: (i) in-situ rainfall
 368 is converted into gridded rainfall through interpolation, and then a grid-to-grid comparison is made; (ii)
 369 gridded data is interpolated to in-situ location and then compared with in-situ data (Nashwan et al.,
 370 2019; Ahmed et al., 2019; Pour et al., 2020d). In the present study, the second approach was used as
 371 the resolution of the remote sensing datasets differed. The satellite rainfall data of the four nearest grid
 372 points of an observed station were interpolated at the observed location using an inverse distance
 373 weighting method and then compared with the observed rainfall. Five statistical metrics were used to
 374 assess the performance of the remote sensing data - normalized root mean square error (*NRMSE*),
 375 percentage of bias (*PBIAS*), ratio of standard deviations (*rSD*), modified index of agreement
 376 (*md*) and Kling-Gupta Efficiency (*KGE*). The formulas, range and optimum values of the
 377 metrics are presented in Table 2.

378

379

380 **Table 2** Description of the statistical metrics used for evaluation of remote sensing data

Metric Formula	Range	Optimal Value
$NRMSE = 100 * \frac{\sqrt{\frac{1}{n} * \sum_{i=1}^n (y_i - x_i)^2}}{sdv(x_i)}$	0 to ∞	0
$PBIAS = 100 * \frac{\sum_{i=1}^N (y_i - x_i)}{x_i}$	$-\infty$ to $+\infty$	0
$md = 1 - \frac{\sum_{i=1}^n (x_i - y_i)^j}{\sum_{i=1}^n (y_i - \bar{x} + x_i - \bar{x})^j}$	0 to 1	1
$rSD = \frac{sd(x_i)}{sd(y_i)}$	0 to ∞	1
$KGE = 1 - \sqrt{(r - 1)^2 + (\gamma - 1)^2 + (\beta - 1)^2}$	-1 to $-\infty$	1

381

382 where n is the samples number; x_i and y_i refer to the observed and remote sensing data,
 383 respectively for time step i ; sd is the standard deviation; \bar{x} and \bar{y} are the mean of the observed
 384 and remote sensing data, respectively. r is Pearson's correlation of the remote sensing data (y)
 385 and observed data (x), γ represents the bias which is normalized by the standard deviation of
 386 the observed data, and β is a fraction of the coefficient of variation representing spatial
 387 variability.

388

389

390 **4 Results and Discussion**

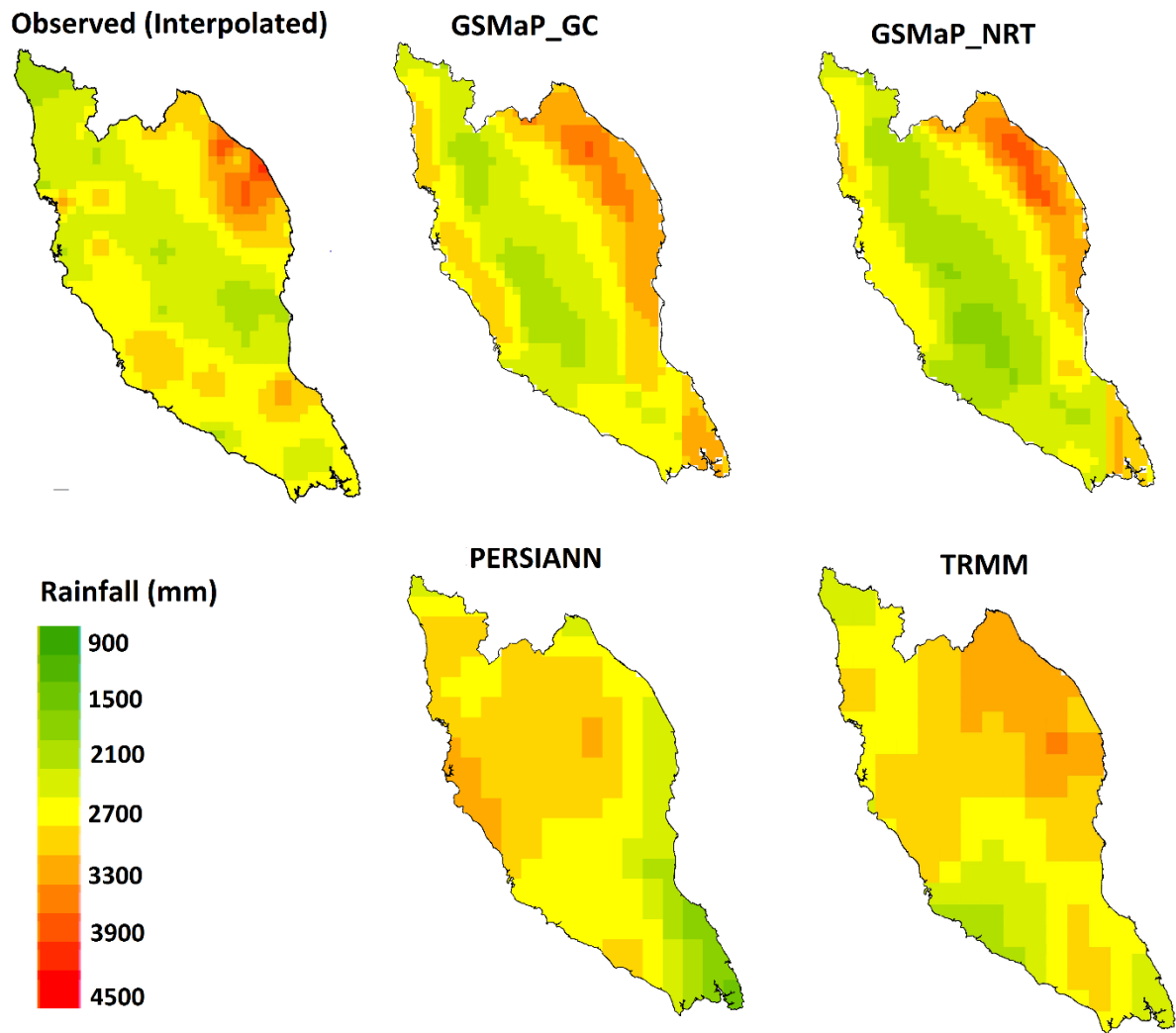
391

392 *4.1 Performance of satellite-based rainfall data products*

393

394 The annual average rainfall figures recorded at 80 rainfall gauges is interpolated to a resolution
 395 of $0.1^\circ \times 1^\circ$ (the finest resolution of the remote sensing data used) using an inverse distance
 396 weighting technique to compare the spatial distribution of the observed and the remotely sensed

397 rainfall (Figure 3). The spatial distribution of GSMaP_NRT and GSMaP_GC rainfall appeared
 398 to have a better match with the spatial distribution of the observed rainfall than those of
 399 PERSIANN and TRMM. However, the GSMaP_NRT results were found to overestimate the
 400 annual rainfall at more grid points when compared to GSMaP_GC. PERSIANN and TRMM
 401 were found to underestimate the annual rainfall in the northeast high rainfall regions and
 402 overestimate the rainfall in most other areas.
 403



404
 405

406 **Figure 3:** Annual average rainfall in Peninsular Malaysia derived from observed and satellite
 407 data products for the period 2000-2018

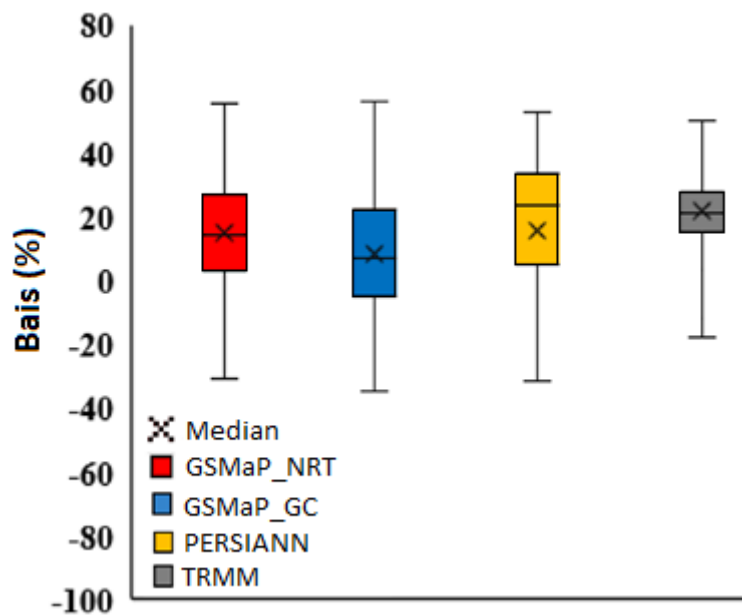
408

409 The bias percent in the median value of the annual average of remotely sensed rainfall data is
 410 shown in the boxplots in Figure 4. The results show an overestimation of rainfall by all the
 411 remote sensing precipitation data. The overestimation in median precipitation was 14.1% for

412 GSMaP_NRT, 7.2% for GSMaP_GC, 23.9% for PERSIANN and 21.2% for TRMM_3B42V7.
413 Overall, the results indicate a better performance by GSMaP_GC in replicating the spatial
414 distribution of annual average Malaysian rainfall, with the least bias. However, the range of
415 bias in GSMaP_GC at different grid points was higher than for the other precipitation products.
416 This indicates a wide variation in the spatial performance of GSMaP_GC in Peninsular
417 Malaysia.

418
419 Previous studies conducted on remote sensing precipitation products in the study area have also
420 reported an overestimation of rainfall. Zad et al. (2018) looked at the performance of
421 TRMM_3B42V7 in the Pahang river basin of Peninsular Malaysia and reported an overestimation
422 of daily rainfall by TRMM at most locations. Tan et al. (2015) also reported an overestimation
423 of rainfall by TRMM and PERSIANN-CDR. Giarno et al. (2018) evaluated the performance
424 of TRMM satellite rainfall products over the Makassar Strait in Indonesia and also reported an
425 overestimation of rainfall.

426



427

428

429 **Figure 4** Percent of bias in median of annual average of remotely sensed rainfall data

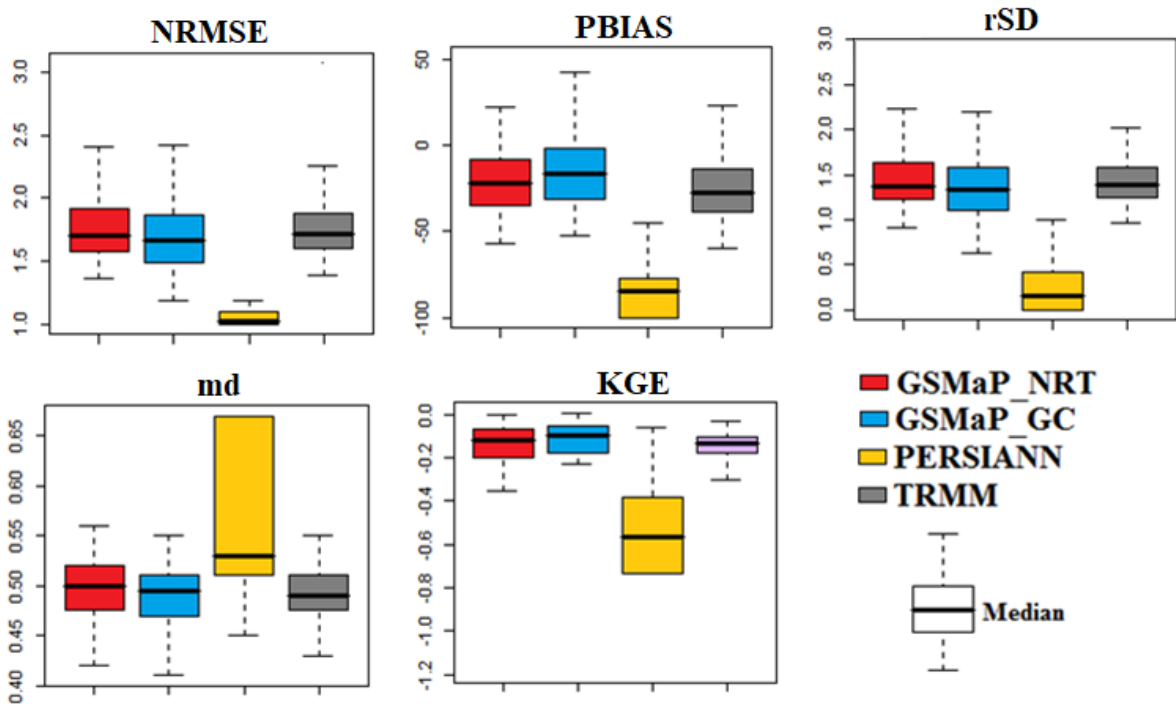
430

431 The time series of observed and remote sensing data at all 80 grid points were compared in
432 order to evaluate the capability of remote sensing data to replicate the observed time series.
433 The results are presented in Figure 5. The GSMaP_GC indicated less NRMSE and PBIAS in
434 comparison to the other products. Three other statistical metrics of GSMaP_GC were also

435 found to be nearer to the optimum value when compared to other products. In construction,
 436 PERSIANN performed the worst of the four products in term of all statistical metrics.

437

438 Hur et al. (2018) compared the performance of TRMM and GSMaP_GC rainfall in Singapore
 439 and reported both products were unable to replicate the observed rainfall, although overall
 440 GSMaP performed more effectively than TRMM. Islam (2018) compared six remote sensing
 441 products over Bangladesh including PERSIANN, CMORPH, IMERG (non-gauge-calibrated
 442 and gauge-calibrated), and GSMaP_NRT and GSMaP-GC. GSMaP_GC performed best, while
 443 PERSIANN was the worst performer.



444

445 **Figure 5** A comparison of time series of remote sensing rainfall data with observed rainfall
 446 data at all the 80 observed locations.

447

448 4.2 Fitting PDF and Estimation of PDF Parameters

449

450 An evaluation was conducted on the performance of the four PDFs and four parameter
 451 estimators using negative log likelihood goodness-of-fit tests. Annual maximum rainfall
 452 amount of 1, 3, 6, 12, 24, 48 and 72-hour durations for the PDFs and parameter estimation
 453 methods were assessed at all eighty stations. Log-likelihood estimates for one location in the
 454 southern peninsular (station Johor 2025001) are presented in Table 2. The GEV distribution

455 and MLE estimator provided the lowest log-likelihood estimates for rainfall amount of all
 456 durations. No significant variation was observed in the log-likelihood estimates for MLE,
 457 GMLE and L-moment approaches. For most of the cases MLE provided the least likelihood
 458 values for estimating the distribution parameters.

459

460 The best PDF and parameter estimator of rainfall of different duration is shown in Figure 6.
 461 Results revealed that GEV is the most suitable PDF with MLE is the best parameter estimation
 462 method at most of the stations. The GEV distribution with MLE estimator provided the least
 463 log-likelihood estimates at 62% of the stations, followed by GEV with a GMLE estimator at
 464 14% of the stations. The GP distribution with MLE at 11%, Exponential with MLE at 5%,
 465 GEV with L-moments at 4% and Gumbel with MLE at 4% of the stations. Therefore, the
 466 rainfall properties were fitted with GEV and the distribution parameters were estimated using
 467 the MLE method for the generation of the IDF curves.

468

469 Based on the goodness of fit test, most suitable PDF was selected using the annual maximum
 470 of observed rainfall data in this work. The PDF selected was fitted to annual maximum of both
 471 observed and remote sensing rainfall data for developing IDF curves for observed and remote
 472 sensing data. Therefore, it is suggested to compare various PDFs separately for developing
 473 remote sensing IDF curves in the future.

474

475 **Table 2** Results of goodness-of-fit test for different probability distribution functions and
 476 parameter estimation methods for rainfall amounts of differing duration at a location in
 477 Southern Malaysia (station Johor 2025001)

Estimator	Distribution	Duration (hours)						
		1	3	6	12	24	48	72
MLE	GEV	175.25	194.05	199.39	202.48	206.24	216.27	217.67
	Gumbel	279.44	299.13	304.49	307.05	309.87	322.57	323.93
	Exp	222.61	238.37	241.84	244.98	249.55	257.89	263.14
	GP	296.27	330.07	343.16	354.56	374.85	358.47	356.47
GMLE	GEV	185.62	197.89	203.30	204.28	212.53	219.23	222.62
	Gumbel	279.44	299.13	304.49	307.05	309.87	322.57	323.93
	Exp	222.61	238.37	241.84	244.98	249.55	257.89	263.14
	GP	487.07	495.39	493.95	496.71	498.34	478.35	491.01
L-Moments	GEV	440.55	669.89	733.69	808.03	744.84	817.29	882.53
	Gumbel	∞	∞	∞	∞	∞	∞	∞
	Exp	∞	∞	∞	∞	∞	∞	∞
	GP	487.07	495.39	493.95	496.71	498.34	478.35	491.01
Bayesian	GEV	436.67	669.32	763.45	753.54	703.70	777.73	793.23

Gumbel	∞	∞	∞	∞	∞	∞	∞
Exp	∞	∞	∞	∞	∞	∞	∞
GP	∞	∞	∞	∞	∞	∞	∞

478

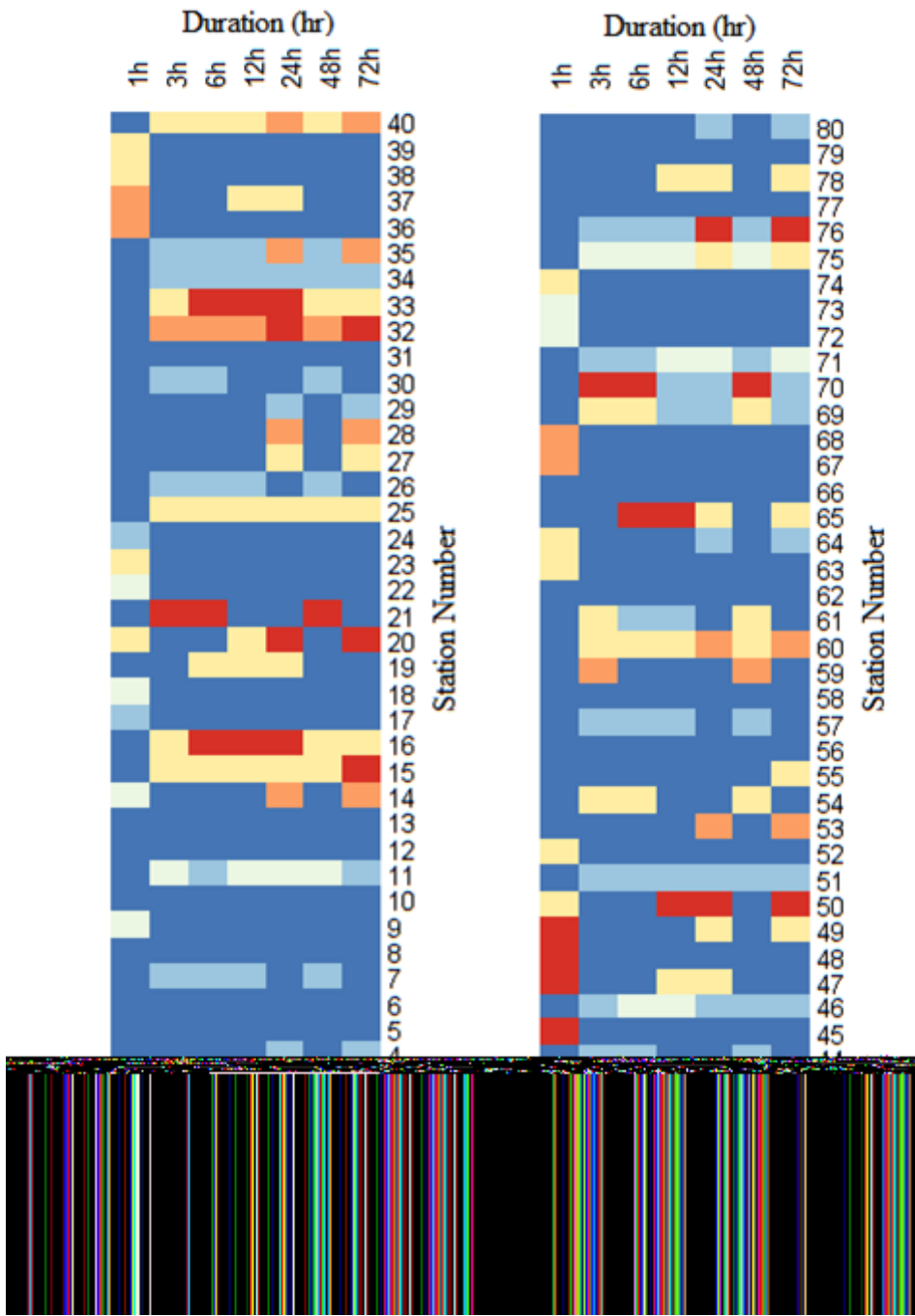
479

480 *4.3 Development of IDF curves*

481

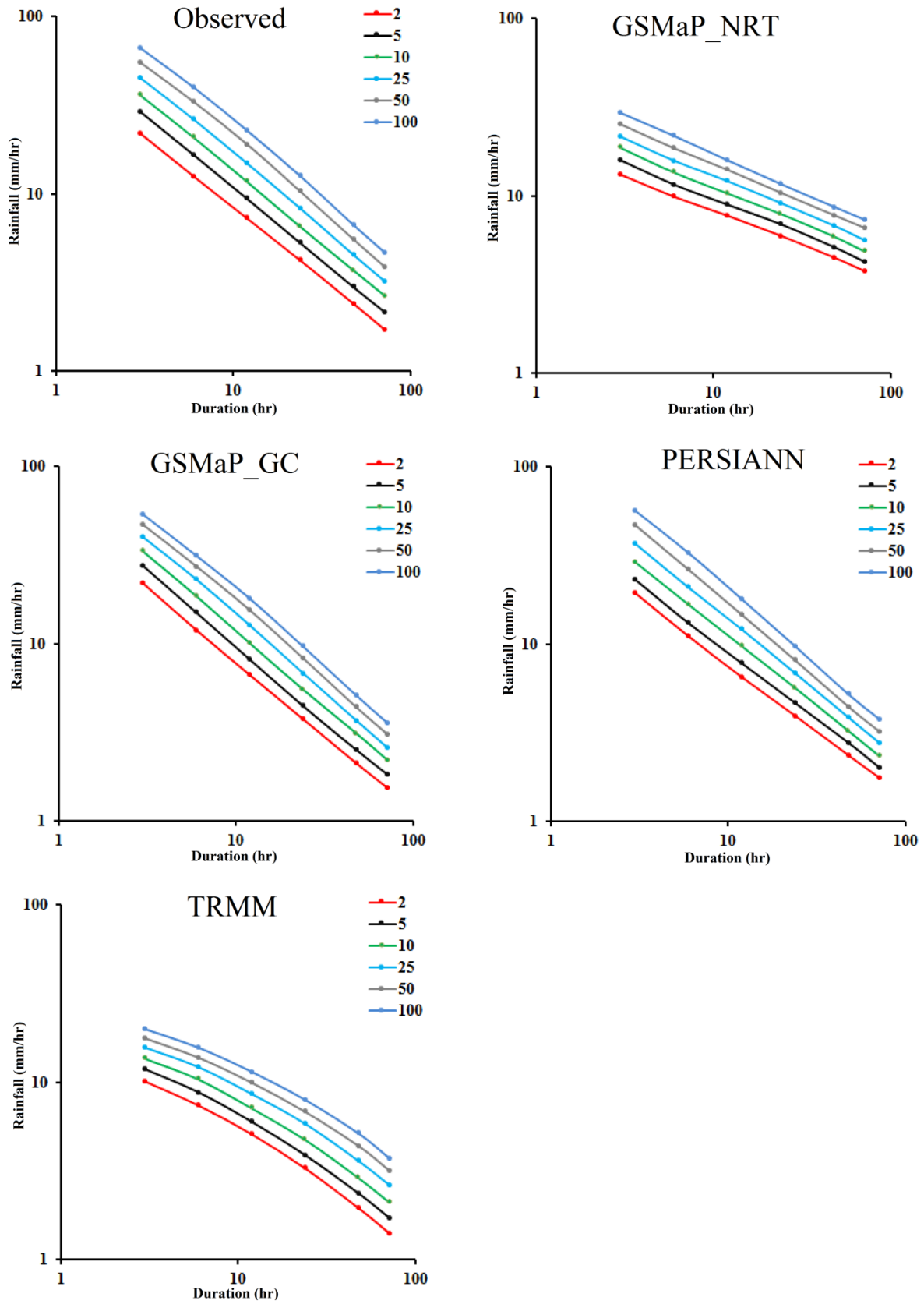
482 IDF curves were developed using both hourly observed and satellite rainfall data for the
 483 period 2000-2018 at all 80 stations. The curves of Pahang station (ID: 3628001), which is
 484 located in the central region of the Peninsula, are shown in Figure 7. The y-axis represents
 485 rainfall intensity (in mm/hr) and the x-axis indicates duration (in hours). IDF curves for
 486 different return periods are also presented. An increase in rainfall intensity with different
 487 return periods and a decrease in rainfall intensity with duration is noted (Figure 7). The
 488 result of one station is shown as an example.

489



490
 491
 492
 493
 494

Figure 6 Best fitted probability distribution function (PDF) for different rainfall periods and most suitable parameter estimation method



495

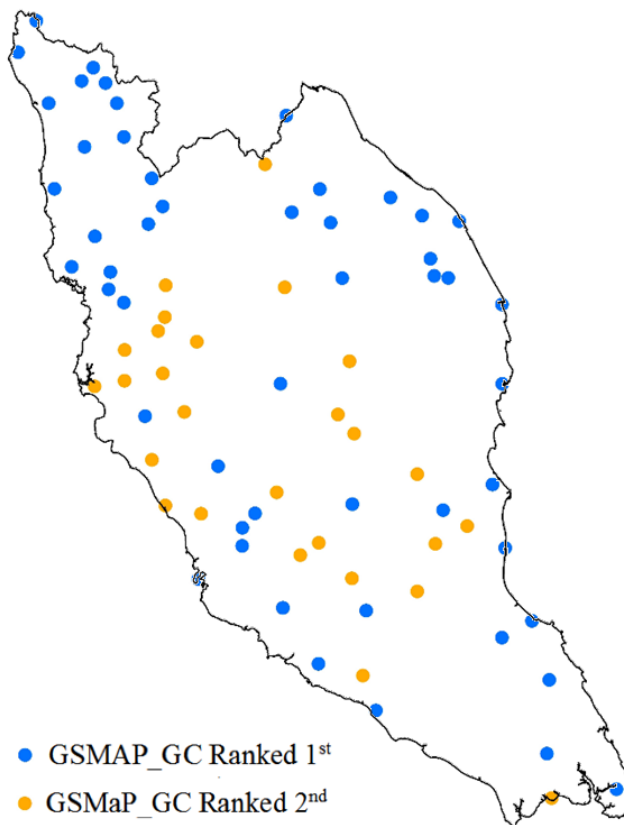
496 **Figure 7** IDF curves for Pahang station (ID: 3628001), showing suitable PDF and
 497 parameter estimate

498

499 4.4 Assessing the performance of remotely-sensed products

500

501 IDF curves, developed using both remotely sensed and observed rainfall data, were compared
502 in order to estimate the bias in the IDF curves generated using the satellite-derived rainfall. The
503 bias in median rainfall intensity for all durations was estimated. The bias of different remote
504 sensing precipitation products was then used to rank the products at the different stations. The
505 remote sensing precipitation data which best replicated the observed IDF curves is presented
506 in Figure 8. The best precipitation product for estimating IDF curves was found to be
507 GSMaP_GC (at 51 of the 80 stations, or 66%), followed by GSMaP_NRT (34%). The
508 PERSIAN and TRMM_3H42V7 products did not perform well at any of the locations. In
509 Figure 8 shows locations at which GSMaP_GC ranked 1st (blue) and at which GSMP_GC
510 ranked 2nd (yellow). GSMaP_GC performed next to GSMaP_NRT at the locations, where
511 GSMaP_NRT performed best. Similarly, GSMaP_NRT performed next to GSMaP_GC at the
512 locations, where GSMaP_GC was found to perform best. The TRMM_3B42V7 product
513 showed a high bias in its IDF curves.

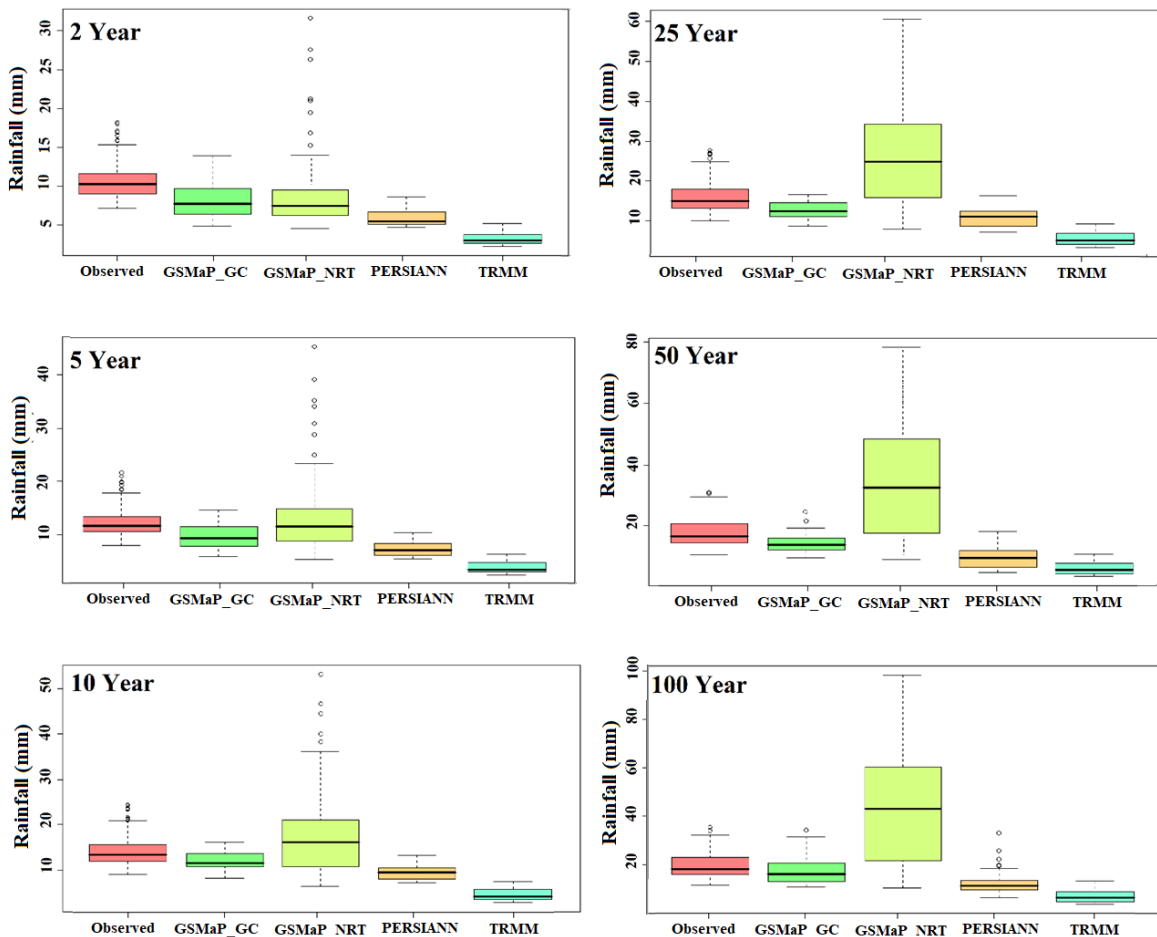


514

515 **Figure 8** Remote sensing precipitation product ranking in the replication of observed IDF
516 curves at different rain gauge locations

517

518 The performance of IDF curves estimated using remote sensing precipitation was assessed by
 519 comparing them with IDF curves estimated using the observed rainfall. Rainfall intensity for
 520 different return periods using the observed and remote sensing precipitation data are presented
 521 in Figure 9. The results show that rainfall intensity for different duration estimated using
 522 GSMaP_GC was most similar to in-situ rainfall intensity for all return periods. A large
 523 difference was observed between GSMaP_NRT and the observed rainfall intensity for all the
 524 return periods (except for the 2-year period). GSMaP_NRT was found to overestimate the
 525 rainfall intensity for ≥ 10 -year return periods. PERSIANN and TRMM appeared to
 526 underestimate rainfall intensity for all return periods. Previous studies have also reported an
 527 underestimation of high rainfall using remote sensing precipitation products (Hur et al., 2018;
 528 Sharifi et al., 2019, Peng et al., 2020, Yao et al., 2020, Liu et al., 2019, Mahmoud et al., 2019).
 529

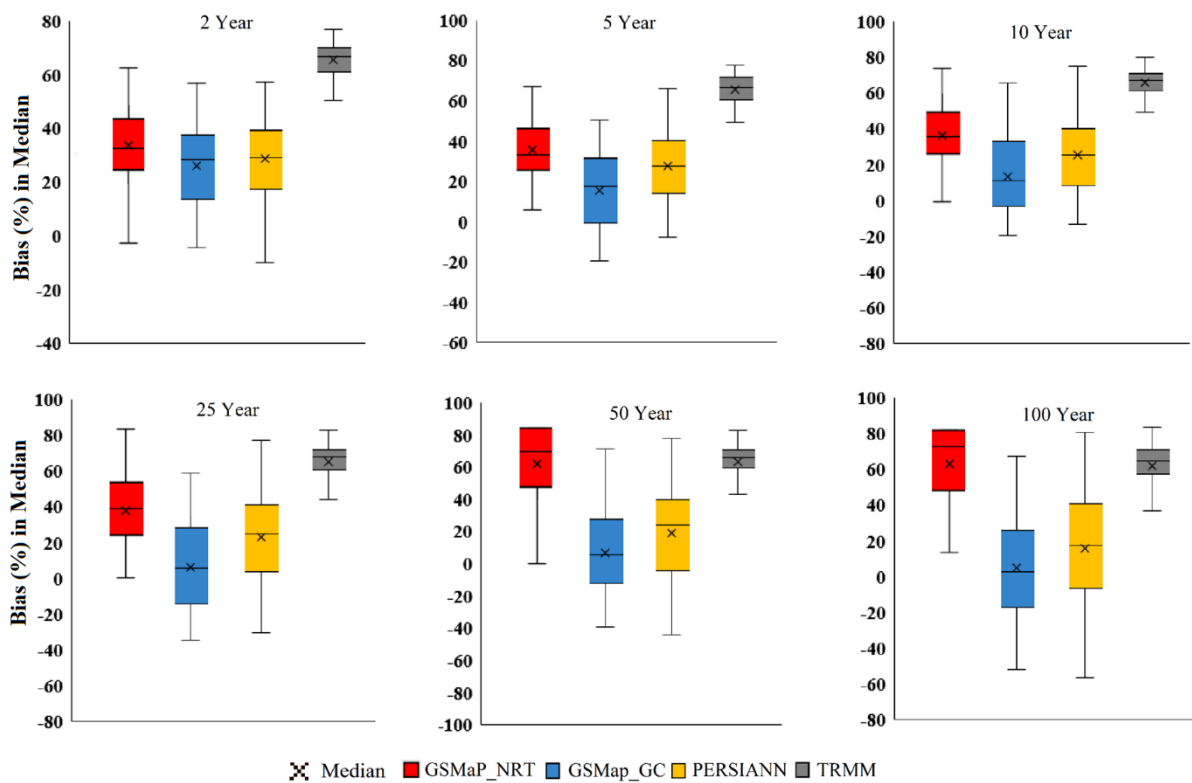


530
 531 **Figure 9** Rainfall intensity at different return periods estimated using observed and remotely
 532 sensed rainfall data

533 The percentage of bias in the median rainfall intensity for different durations at all locations
 534 were calculated and are presented in Figure 10. The figures clearly show that all of the remote

535 sensing precipitation data underestimated rainfall intensity of all durations, with the exception
 536 of GSMaP_NRT for the higher return periods (>10-year). GSMaP_GC was found to be the
 537 best performer, (underestimating by 8–27%) followed by PERSIANN (28–32%) and
 538 GSMaP_NRT (35–49%). The underestimation was highest for TRMM_3B42V7 (65–67%).
 539 Bias in GSMaP_GC was found to be less (8-12%) for the higher return periods (>10-year) and
 540 also high for the lower return periods (18-27%). The bias in other rainfall product was
 541 consistently high for all return periods.

542



543

544

545 **Figure 10** Percent of bias in median intensity of remote sensing rainfall for different return
 546 periods at all stations

547

548 It has been reported that most of the remote sensing precipitation products overestimate light
 549 rainfall and underestimate high rainfall (Sharifi et al., 2019, Peng et al., 2020, Yao et al., 2020,
 550 Liu et al., 2019, Mahmoud et al., 2019). This causes a high bias in IDF curve estimated using
 551 remote sensing precipitation data. Sun et al. (2019) used remote sensing rainfall for developing
 552 IDF curves in Singapore and reported 70% bias in remote sensing based IDF curves compared
 553 to observed IDF curves. Ombadi et al. (2018) evaluated the performance of PERSIANN-CDR

554 against NOAA Atlas 14 for estimating IDF curves in the USA, with results showing a median
555 bias of between 3 and 22% for precipitation durations of one to three days.

556

557 Rainfall intensity for different durations at all stations was used to evaluate individual
558 performances using a Taylor diagram (Taylor, 2001). The results are presented in Figure 11.
559 The circle in black located on the x-axis represents the observed rainfall while filled circles
560 with different colours denote precipitation based on remote sensing products. The diagram
561 shows the performance of datasets based on similarity in correlation and variability. The circle
562 nearest to the observed one represents the best product. The analysis shows good performance
563 of the GSMaP_GC rainfall product for lower return periods (<10-year), with an almost similar
564 performance for higher return periods.

565

566 A gradual decrease in correlation with return period was observed. This is mainly due to a
567 higher bias in the rainfall intensity of the higher return periods. Similar results were also found
568 by Marra et al. (2017a) when comparing radar and satellite (CMORPH) IDF curves in the East
569 Mediterranean region; specifically a high correlation for shorter return period, and then a
570 gradual decrease in correlation with increasing return periods.

571

The picture can't be displayed.

572

573 **Figure 11** Taylor diagram, showing performance of different remote sensing rainfall products

574 in replicating observed rainfall intensity at different return periods

575

576 The study revealed a high bias in the IDF curves which were estimated using the remote sensing
577 data, with the least bias being shown by GSMaP_GC. The bias in GSMaP_GC for return
578 periods >10-year was 8-12%, while it was a bit higher for the lower return periods (18-27%).
579 This indicates that GSMaP_GC rainfall can be used for generating IDF curves once the small
580 amount of bias has been corrected. The study revealed that the good performance of remote
581 sensing rainfall data in terms of their ability to replicate annual or seasonal rainfall totals, or
582 the actual spatial distribution of rainfall, does not mean that this data can be used to provide a
583 better estimation of the IDF curves. The reliability of the remote sensing rainfall data should
584 be based on their ability to reproduce reliable observed IDF curves.

585

586 *4.5 Spatial distribution of bias*

587

588 Sixty-four of the 80 stations (80% stations) were randomly selected for estimation of the spatial
589 distribution of bias in GSMaP_GC rainfall intensity for differing return periods. The remaining
590 16 stations (20% of the total) were used to assess the performance of the bias-corrected IDF
591 curves at defined ungauged locations. Though the bias in the median was less for higher return
592 periods and high for lower return periods, the spatial variability of bias was reduced for the
593 lower return periods and increased for the higher return periods (Figure 12). The bias was found
594 to be higher in the coastal areas and lower in the central region. The highest bias in rainfall
595 intensity for all return periods was found in the northeast. Rainfall intensity in this region is
596 high compared to other regions. As the GSMaP_GC rainfall failed to capture the high rainfall
597 intensity, the bias is therefore very high.

598

599 The biases in remote sensing rainfall data depend on various physiographic factors. This
600 includes topography, elevation and proximity to shorelines, as well as climatic factors such as
601 wind speed and cloud cover type (Yao et al., 2020, Kalimeris and Kolios, 2019, Cavalcante et
602 al., 2020, Sobral et al., 2020). Future studies should concentrate on correlating specific
603 physiographic and climatic factors with the noted bias in remote sensed rainfall in order to
604 better understand the various factors affecting the bias. These factors can then be incorporated
605 into a bias correction process to provide a better estimation of IDF curves generated from
606 remotely sensed precipitation products.

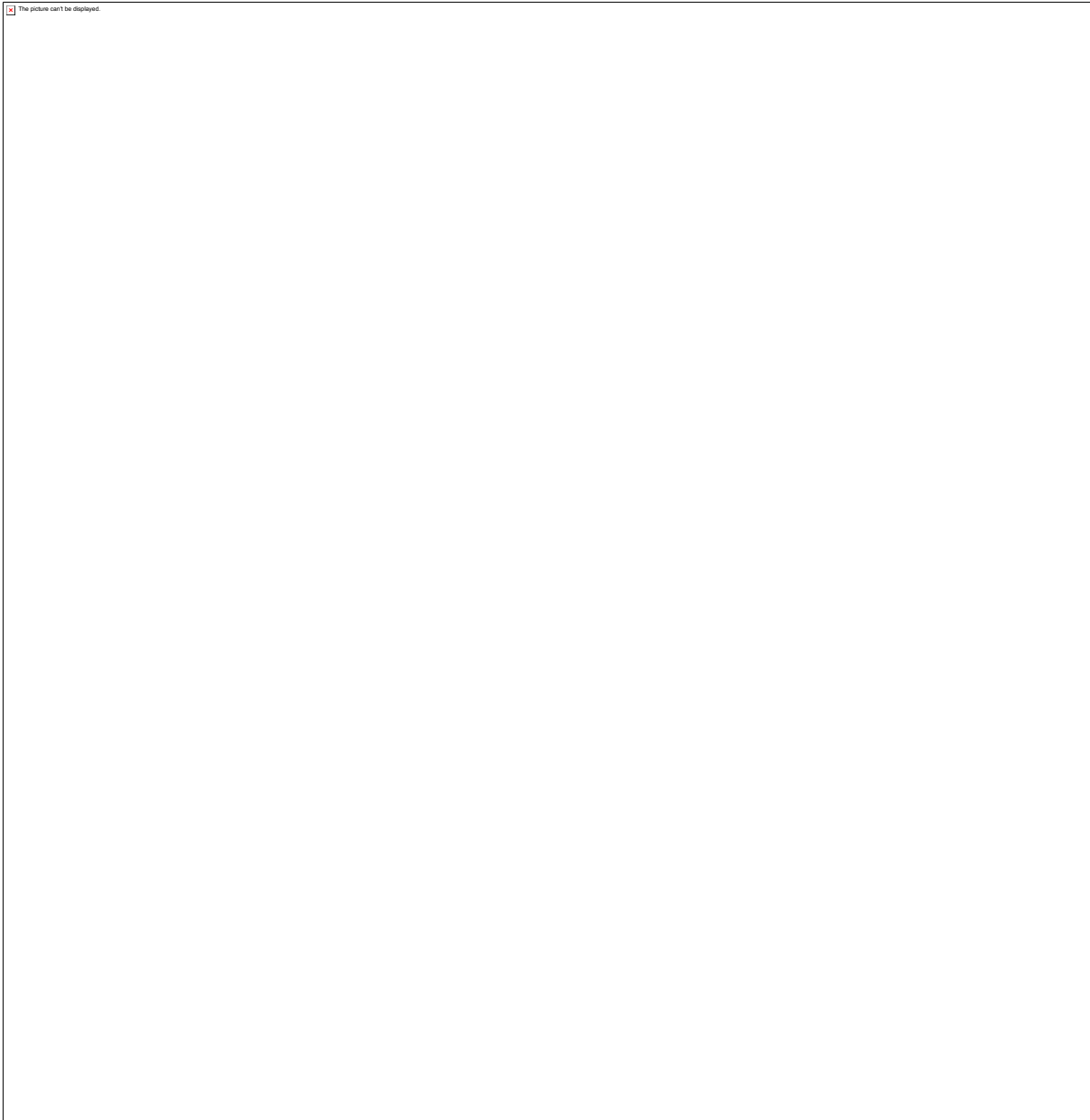
607

608

609
610
611
612
613
614
615
616
617
618
619
620
621
622
623
624
625
626
627

4.6 Performance bias corrected IDF curves

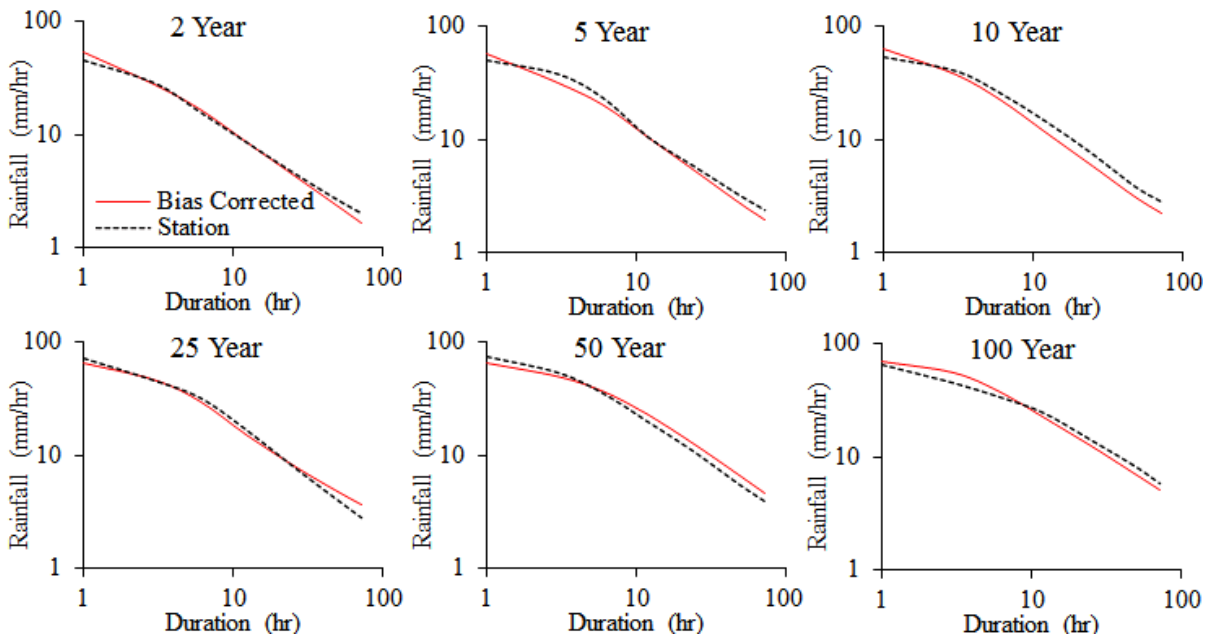
Bias estimates for the 16 stations not used to estimate the spatial distribution of bias (Figure 12) were used to assess the performance of the bias-corrected GSMaP_GC IDF curves at ungauged locations. An example of the evaluation results for the observed and bias-corrected GSMaP_GC IDF curves for different return periods of a station located in the south of the peninsula (Johor 2025001) are shown in Figure 13. This shows a good match between observed and bias-corrected GSMaP_GC IDF curves for the different return periods. The graphed results are presented in Figure 14, showing a perfect match in rainfall intensity between observed and GSMaP_GC data. The respective median values agree well for the lower return periods (<10-year). The bias in the median of the rainfall intensity of GSMaP_GC for the higher return periods was also found to be very close to the intensity of the observed rainfall and the range of rainfall intensity for the different return periods was also found to match well. These results indicate that the bias-corrected IDF curves derived from GSMaP_GC rainfall are eminently suitable for hydrological studies and hydraulic design work.



628

629 **Figure 12** Spatial distribution of bias in GSMaP_CG rainfall intensity for different return
630 periods

631



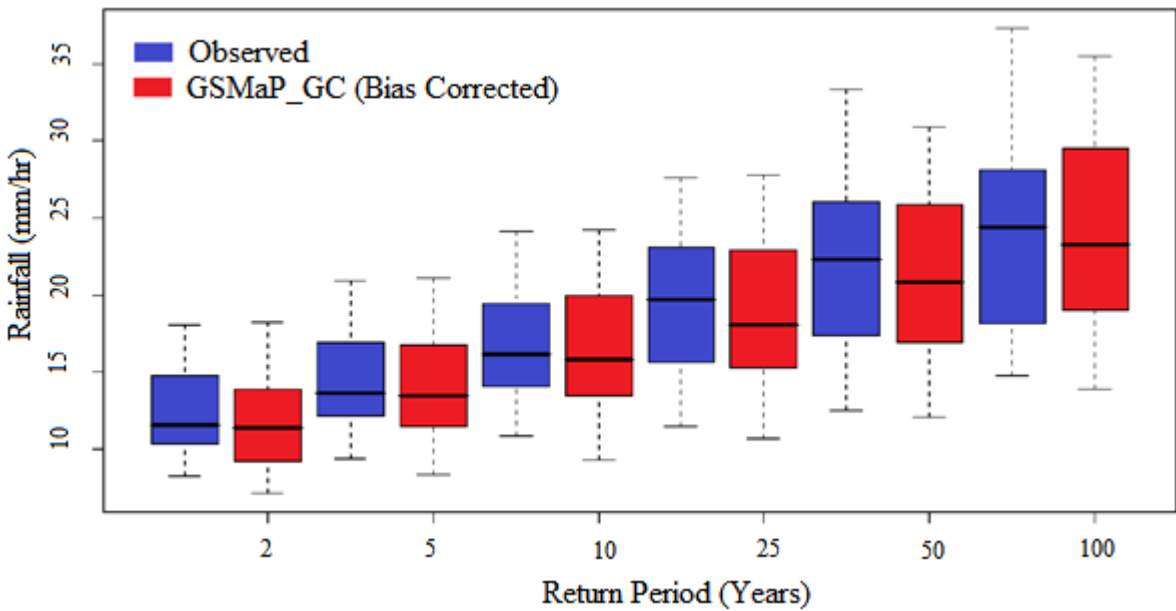
632

633

634 **Figure 13** Observed and bias-corrected GSMaP_CG IDF curves for different return periods of
635 a station located in the south of the Peninsula

636

637



638

639 **Figure 14** Observed and GSMaP_GC rainfall intensity after bias-correction for different return
640 periods

641

642 **5. Conclusion**

643

644 In a study, four satellite-derived rainfall data products were evaluated to determine their ability
645 to replicate IDF curves in Peninsular Malaysia. An analysis of the initial results indicated that
646 all the remote sensing rainfall underestimated the rainfall intensities for different durations and
647 return periods. When the results were corrected for bias, however, the outcomes looked more
648 promising. This shows that the correction for bias is essential when generating IDF curves
649 using remote sensing precipitation data. The results indicate that GSMaP_GC is the best
650 product to use for the IDF curves (with an 8-27% bias). The spatial distribution of bias for
651 different rainfall return periods for GSMaP_GC was also generated in this study, and can be
652 used for correction of bias in the IDF curves estimated using GSMaP_GC. This enables use at
653 locations where actual rainfall data is not available and so the procedure used in this study can
654 be used to develop IDF curves in any regions where suitable data is lacking. These study results
655 can be used when designing hydraulic structures in the regions of Peninsular Malaysia where
656 gauged data are unavailable. Biases in remote sensing data can be corrected before being use
657 in IDF curve development and compared with the results obtained in this study. The
658 performance of different bias correction methods can be evaluated to improve the performance
659 of remote sensing rainfall in generating IDF curves. The best PDFs can be estimated for both
660 observed and remote sensing data when preparing corresponding IDF curves to allow a better
661 comparison with remote sensing rainfall products. The performance of remote sensing data
662 based on different rainfall extremes such as intensity, duration and frequency can also be
663 evaluated. Besides, the performance of other high-resolution satellite-based rainfall products
664 that offer data for shorter period can be compared and evaluated.

665

666

667

668

669 **References**

- 670 ABBASPOUR, K. C., ROUHOLAHNEJAD, E., VAGHEFI, S., SRINIVASAN, R., YANG,
671 H. & KLØVE, B. 2015. A continental-scale hydrology and water quality model for Europe:
672 Calibration and uncertainty of a high-resolution large-scale SWAT model. *Journal of*
673 *Hydrology*, 524, 733-752.
- 674 AL-AMRI, N. S. & SUBYANI, A. M. 2017. Generation of rainfall intensity duration frequency
675 (IDF) curves for ungauged sites in arid region. *Earth Systems and Environment*, 1, 8.
- 676 ALIJANIAN, M., RAKHSHANDEHROO, G. R., MISHRA, A. K., DEHGHANI, M. (2017).
677 Evaluation of Satellite Rainfall Climatology Using CMORPH, PERSIANN-CDR,
678 PERSIANN, TRMM, MSWEP Over Iran. *International Journal of Climatology*. DOI:
679 10.1002/Joc.5131
- 680 ALMAZROUI, M. & SAEED, S. 2020. Contribution of extreme daily precipitation to total
681 rainfall over the Arabian Peninsula. *Atmospheric Research*, 231, 104672.
- 682 ALMAZROUI, M., ŞEN, Z., MOHORJI, A.M. et al. 2019. Impacts of Climate Change on
683 Water Engineering Structures in Arid Regions: Case Studies in Turkey and Saudi Arabia. *Earth*
684 *System Environment*, 3, 43–57 (2019). <https://doi.org/10.1007/s41748-018-0082-6>
- 685 ASHOURI, H., HSU, K.-L., SOROOSHIAN, S., BRAITHWAITE, D. K., KNAPP, K. R.,
686 CECIL, L. D., NELSON, B. R. & PRAT, O. P. 2015. PERSIANN-CDR: Daily precipitation
687 climate data record from multisatellite observations for hydrological and climate studies.
688 *Bulletin of the American Meteorological Society*, 96, 69-83.
- 689 BELO-PEREIRA, M., DUTRA, E. & VITERBO, P. 2011. Evaluation of global precipitation
690 data sets over the Iberian Peninsula. *Journal of Geophysical Research: Atmospheres*, 116.
- 691 BIERMAN, G., BELZER, M. R., VANDERGRAFT, J. S. & PORTERT, D. Maximum
692 likelihood estimation using square root information filters. 1989 American Control
693 Conference, 1989. IEEE, 2646-2652.
- 694 BOSMAN, P. A. & THIERENS, D. 2000. Negative log-likelihood and statistical hypothesis
695 testing as the basis of model selection in IDEAs.
- 696 CAVALCANTE, R. B. L., DA SILVA FERREIRA, D. B., PONTES, P. R. M., TEDESCHI,
697 R. G., DA COSTA, C. P. W. & DE SOUZA, E. B. 2020. Evaluation of extreme rainfall indices
698 from CHIRPS precipitation estimates over the Brazilian Amazonia. *Atmospheric Research*,
699 238, 104879.
- 700 CHEN, F. & LI, X. 2016. Evaluation of IMERG and TRMM 3B43 monthly precipitation
701 products over mainland China. *Remote Sensing*, 8, 472.
- 702 CHEN, S., HONG, Y., CAO, Q., KIRSTETTER, P.-E., GOURLEY, J. J., QI, Y., ZHANG, J.,
703 HOWARD, K., HU, J. & WANG, J. 2013. Performance evaluation of radar and satellite
704 rainfalls for Typhoon Morakot over Taiwan: Are remote-sensing products ready for gauge
705 denial scenario of extreme events? *Journal of hydrology*, 506, 4-13.
- 706 CHOW, V. T., MAIDMENT, D. R. & MAYS, L. W. 1988. *Applied hydrology*.

707 COURTY, L. G., WILBY, R. L., HILLIER, J. K. & SLATER, L. J. 2019. Intensity-duration-
708 frequency curves at the global scale. *Environmental Research Letters*, 14, 084045.

709 DE PAOLA, F., GIUGNI, M., TOPA, M. E. & BUCCHIGNANI, E. 2014. Intensity-Duration-
710 Frequency (IDF) rainfall curves, for data series and climate projection in African cities.
711 SpringerPlus, 3, 133.

712 DEWAN, A., HU, K., KAMRUZZAMAN, M. & UDDIN, M. R. 2019. Evaluating the
713 spatiotemporal pattern of concentration, aggressiveness and seasonality of precipitation over
714 Bangladesh with time-series Tropical Rainfall Measuring Mission data. *Extreme*
715 *Hydroclimatic Events and Multivariate Hazards in a Changing Environment*. Elsevier.

716 ENDRENY, T. A. & IMBEAH, N. 2009. Generating robust rainfall intensity-duration-
717 frequency estimates with short-record satellite data. *Journal of Hydrology*, 371, 182-191.

718 FAIZ, M. A., LIU, D., FU, Q., SUN, Q., LI, M., BAIG, F., LI, T. & CUI, S. 2018. How accurate
719 are the performances of gridded precipitation data products over Northeast China?
720 *Atmospheric Research*, 211, 12-20.

721 FIENBERG, S. E. 1997. Introduction to RA Fisher on inverse probability and likelihood.
722 *Statistical Science*, 12, 161-161.

723 FISHER, R. 1912. The maximum-likelihood-method. *Messenger in Mathematics*, 41, 155-
724 160.

725 GOSSET, M., ALCOBA, M., ROCA, R., CLOCHÉ, S. & URBANI, G. 2018. Evaluation of
726 TAPEER daily estimates and other GPM-era products against dense gauge networks in West
727 Africa, analysing ground reference uncertainty. *Quarterly Journal of the Royal Meteorological*
728 *Society*, 144, 255-269.

729 HAJANI, E., RAHMAN, A. & ISHAK, E. 2017. Trends in extreme rainfall in the state of New
730 South Wales, Australia. *Hydrological Sciences Journal*, 62, 2160-2174.

731 HASAN, E., TARHULE, A., HONG, Y. & MOORE, B. 2019. Assessment of physical water
732 scarcity in Africa using GRACE and TRMM satellite data. *Remote Sensing*, 11, 904.

733 HERRERA, S., GUTIÉRREZ, J. M., ANCELL, R., PONS, M., FRÍAS, M. & FERNÁNDEZ,
734 J. 2012. Development and analysis of a 50-year high-resolution daily gridded precipitation
735 dataset over Spain (Spain02). *International Journal of Climatology*, 32, 74-85.

736 HILBE, J. M., & ROBINSON, A. P. (2013). *Methods of statistical model estimation*. CRC
737 Press.

738 HONG, H. P., LI, S. H., & MARA, T. G. (2013). Performance of the generalized least-squares
739 method for the Gumbel distribution and its application to annual maximum wind speeds.
740 *Journal of Wind Engineering and Industrial Aerodynamics*, 119, 121-132.

741 HUANG, W.-R., CHANG, Y.-H. & LIU, P.-Y. 2018. Assessment of IMERG precipitation over
742 Taiwan at multiple timescales. *Atmospheric Research*, 214, 239-249.

743 HUFFMAN, G. J. 2016. The transition in multi-satellite products from TRMM to GPM (TMPA
744 to IMERG). Version 161025, 5.

745 IPCC 2014. IPCC, 2014: Climate Change 2014: Synthesis Report. Contribution of Working
746 Groups I, II and III to the Fifth Assessment Report of the Intergovernmental Panel on Climate
747 Change [Core Writing Team, R.K. Pachauri and L.A. Meyer (eds.)]. IPCC, Geneva,
748 Switzerland, 151 pp. <https://www.ipcc.ch/report/ar5/syr/>.

749 ISLAM, M. A. 2018. Statistical comparison of satellite-retrieved precipitation products with
750 rain gauge observations over Bangladesh. *International Journal of Remote Sensing*, 39, 2906-
751 2936.

752 JENKINSON, A. F. 1955. The Frequency Distribution of The Annual Maximum (or
753 Minimum) Values of Meteorological Elements. *Quarterly Journal of The Royal Meteorological*
754 *Society*, 81, 158-171.

755 JIANG, S., REN, L., ZHOU, M., YONG, B., ZHANG, Y. & MA, M. 2017. Drought
756 monitoring and reliability evaluation of the latest TMPA precipitation data in the Weihe River
757 Basin, Northwest China. *Journal of Arid Land*, 9, 256-269.

758 KALIMERIS, A. & KOLIOS, S. 2019. TRMM-based rainfall variability over the Central
759 Mediterranean and its relationships with atmospheric and oceanic climatic modes.
760 *Atmospheric Research*, 230, 104649.

761 KHAN, N., POUR, S.H., SHAHID, S., ISMAIL, T., AHMED, K., CHUNG, E.S., NAWAZ,
762 N., WANG, X..J., 2019. Spatial distribution of secular trends in rainfall indices of peninsular
763 Malaysia in the presence of long-term persistence. *Meteorl Appl.*
764 <https://doi.org/10.1002/met.1792>

765 KIDD, C., BECKER, A., HUFFMAN, G. J., MULLER, C. L., JOE, P., SKOFRONICK-
766 JACKSON, G. & KIRSCHBAUM, D. B. 2017. So, how much of the Earth's surface is covered
767 by rain gauges? *Bulletin of the American Meteorological Society*, 98, 69-78.

768 KJELDTSEN, T. R., LUNDORF, A., & ROSBJERG, D. (2000). Use of a two-component
769 exponential distribution in partial duration modelling of hydrological droughts in Zimbabwean
770 rivers. *Hydrological Sciences Journal*, 45(2), 285-298.

771 KOUTSOYIANNIS, D., KOZONIS, D. & MANETAS, A. 1998. A mathematical framework
772 for studying rainfall intensity-duration-frequency relationships. *Journal of Hydrology*, 206,
773 118-135.

774 KUMAR, B. & LAKSHMI, V. 2018. Accessing the capability of TRMM 3B42 V7 to simulate
775 streamflow during extreme rain events: Case study for a Himalayan River Basin. *Journal of*
776 *Earth System Science*, 127, 27.

777 LAITI, L., MALLUCCI, S., PICCOLROAZ, S., BELLIN, A., ZARDI, D., FIORI, A.,
778 NIKULIN, G. & MAJONE, B. 2018. Testing the hydrological coherence of high-resolution
779 gridded precipitation and temperature data sets. *Water Resources Research*, 54, 1999-2016.

780 LIEW, S. C., RAGHAVAN, S. V. & LIONG, S.-Y. 2014. Development of Intensity-Duration-
781 Frequency curves at ungauged sites: risk management under changing climate. *Geoscience*
782 *Letters*, 1, 8.

783 LIMA, C. H., KWON, H.-H. & KIM, Y.-T. 2018. A local-regional scaling-invariant Bayesian
784 GEV model for estimating rainfall IDF curves in a future climate. *Journal of Hydrology*, 566,
785 73-88.

786 LIU, J., SHANGGUAN, D., LIU, S., DING, Y., WANG, S. & WANG, X. 2019. Evaluation
787 and comparison of CHIRPS and MSWEP daily-precipitation products in the Qinghai-Tibet
788 Plateau during the period of 1981–2015. *Atmospheric Research*, 230, 104634.

789 MAHMOUD, M. T., HAMOUDA, M. A. & MOHAMED, M. M. 2019. Spatiotemporal
790 evaluation of the GPM satellite precipitation products over the United Arab Emirates.
791 *Atmospheric research*, 219, 200-212.

792 MARRA, F. & MORIN, E. 2015. Use of radar QPE for the derivation of Intensity–Duration–
793 Frequency curves in a range of climatic regimes. *Journal of Hydrology*, 531, 427-440.

794 MARRA, F., MORIN, E., PELEG, N., MEI, Y. & ANAGNOSTOU, E. N. 2017. Intensity-
795 duration-frequency curves from remote sensing rainfall estimates: comparing satellite and
796 weather radar over the eastern Mediterranean. *Hydrology and Earth System Sciences*, 21, 2389-
797 2404.

798 MARRA, F., NIKOLOPOULOS, E., CREUTIN, J. & BORGA, M. 2016. Space–time
799 organization of debris flows-triggering rainfall and its effect on the identification of the rainfall
800 threshold relationship. *Journal of hydrology*, 541, 246-255.

801 MARTINS, E. S., & STEDINGER, J. R. (2000). Generalized maximum-likelihood generalized
802 extreme-value quantile estimators for hydrologic data. *Water Resources Research*, 36(3), 737-
803 744.

804 MAYOWA, O. O., POUR, S. H., SHAHID, S., MOHSENIPOUR, M., HARUN, S. B.,
805 HERYANSYAH, A. & ISMAIL, T. 2015. Trends in rainfall and rainfall-related extremes in
806 the east coast of peninsular Malaysia. *Journal of Earth System Science*, 124, 1609-1622.

807 MISSION, T. R. M. 2011. TRMM (TMPA) Rainfall Estimate L3 3 hour 0.25 degree x 0.25
808 degree V7, Greenbelt, MD, Goddard Earth Sciences Data and Information Services Center
809 (GES DISC). TRMM_3B42_7. html.

810 NASHWAN, M. & SHAHID, S. 2019a. Spatial distribution of unidirectional trends in climate
811 and weather extremes in Nile river basin. *Theoretical and Applied Climatology*, 137, 1181–
812 1199.

813 NASHWAN, M. S. & SHAHID, S. 2019b. Symmetrical uncertainty and random forest for the
814 evaluation of gridded precipitation and temperature data. *Atmospheric Research*, 230, 104632.

815 NASHWAN, M. S., SHAHID, S. & RAHIM, N. A. 2019. Unidirectional trends in annual and
816 seasonal climate and extremes in Egypt. *Theoretical and Applied Climatology*, 136, 457-473.

817 NASHWAN, M., SHAHID, S., CHUNG, E.-S., AHMED, K. & SONG, Y. 2018. Development
818 of climate-based index for hydrologic hazard susceptibility. *Sustainability*, 10, 2182.

819 NGUYEN, P., OMBADI, M., SOROOSHIAN, S., HSU, K., AGHAKOUCHAK, A.,
820 BRAITHWAITE, D., ASHOURI, H. & THORSTENSEN, A. R. 2018. The PERSIANN family

821 of global satellite precipitation data: a review and evaluation of products. *Hydrology and Earth*
822 *System Sciences*, 22, 5801-5816.

823 NOOR, M., ISMAIL, T., SHAHID, S., NASHWAN, M. S. & ULLAH, S. 2019. Development
824 of multi-model ensemble for projection of extreme rainfall events in Peninsular Malaysia.
825 *Hydrology Research*, 50, 1772-1788.

826 OKAMOTO, K. I., USHIO, T., IGUCHI, T., TAKAHASHI, N. & IWANAMI, K. 2005. The
827 Global Satellite Mapping of Precipitation (GSMaP) project.

828 OMBADI, M., NGUYEN, P., SOROOSHIAN, S. & HSU, K. L. 2018. Developing Intensity-
829 Duration-Frequency (IDF) Curves from Satellite-Based Precipitation: Methodology and
830 Evaluation. *Water Resources Research*, 54, 7752-7766.

831 OVEREEM, A., BUIHAND, T. & HOLLEMAN, I. 2009. Extreme rainfall analysis and
832 estimation of depth-duration-frequency curves using weather radar. *Water resources research*,
833 45.

834 PALOMINO-ÁNGEL, S., ANAYA-ACEVEDO, J. A. & BOTERO, B. A. 2019. Evaluation of
835 3B42V7 and IMERG daily-precipitation products for a very high-precipitation region in
836 northwestern South America. *Atmospheric Research*, 217, 37-48.

837 PANZIERA, L., GABELLA, M., ZANINI, S., HERING, A., GERMANN, U. & BERNE, A.
838 2016. A radar-based regional extreme rainfall analysis to derive the thresholds for a novel
839 automatic alert system in Switzerland. *Hydrology and earth system sciences*, 20, 2317-2332.

840 PELEG, N., MARRA, F., FATICHI, S., PASCHALIS, A., MOLNAR, P. & BURLANDO, P.
841 2018. Spatial variability of extreme rainfall at radar subpixel scale. *Journal of Hydrology*, 556,
842 922-933.

843 PENG, J., DADSON, S., HIRPA, F., DYER, E., LEES, T., GONZALEZ MIRALLES, D.,
844 VICENTE-SERRANO, S. M. & FUNK, C. 2020. A pan-African high-resolution drought index
845 dataset. *Earth System Science Data*, 12, 753-769.

846 POUDEL, K. P. & CAO, Q. V. 2013. Evaluation of methods to predict Weibull parameters for
847 characterizing diameter distributions. *Forest Science*, 59, 243-252.

848 POUR, S.H., HARUN, S., SHAHID, S. 2014. Genetic Programming for the Downscaling of
849 Extreme Rainfall Events on the East Coast of Peninsular Malaysia. *Atmosphere*, 2014(5), 914-
850 936

851 POUR, S.H., WAHAB, A.K.A., Shahid, S. Ismail, Z.B. 2020a. Changes in reference
852 evapotranspiration and its driving factors in peninsular Malaysia. *Atmospheric Research*, 249,
853 105096. <https://doi.org/10.1016/j.atmosres.2020.105096>

854 POUR, S.H., WAHAB, A.K.A., SHAHID, S., ASADUZZAMAN, M., DEWAN, A. 2020b. Low
855 impact development techniques to mitigate the impacts of climate-change-induced urban floods:
856 Current trends, issues and challenges. *Sustainable Cities and Society*, 62, 102373.
857 <https://doi.org/10.1016/j.scs.2020.102373>

858 POUR, S.H., WAHAB, A.K.A, SHAHID, S. 2020c. Physical-empirical models for prediction
859 of seasonal rainfall extremes of Peninsular Malaysia. *Atmospheric Research*, 233, 104720.
860 <https://doi.org/10.1016/j.atmosres.2019.104720>

861 POUR, S.H, WAHAB, A.K.A., Shahid, S. 2020d. Spatiotemporal changes in precipitation
862 indicators related to bioclimate in Iran. *Theoretical and Applied Climatology*. DOI:
863 10.1007/s00704-020-03192-6.

864 PRAKASH, S., MITRA, A. K., MOMIN, I. M., RAJAGOPAL, E. N., BASU, S., COLLINS,
865 M., TURNER, A. G., ACHUTA RAO, K. & ASHOK, K. 2015. Seasonal intercomparison of
866 observational rainfall datasets over India during the southwest monsoon season. *International*
867 *Journal of Climatology*, 35, 2326-2338.

868 PREIN, A. F. & GOBIET, A. 2017. Impacts of uncertainties in European gridded precipitation
869 observations on regional climate analysis. *International Journal of Climatology*, 37, 305-327.

870 RAHMAN, A. S., RAHMAN, A., ZAMAN, M. A., HADDAD, K., AHSAN, A. & IMTEAZ,
871 M. 2013. A study on selection of probability distributions for at-site flood frequency analysis
872 in Australia. *Natural hazards*, 69, 1803-1813.

873 REDDY, M. V., MITRA, A. K., MOMIN, I. M., MITRA, A. K. & PAI, D. 2019. Evaluation
874 and inter-comparison of high-resolution multi-satellite rainfall products over India for the
875 southwest monsoon period. *International journal of remote sensing*, 40, 4577-4603.

876 REIS JR, D. S., & STEDINGER, J. R. (2005). Bayesian MCMC flood frequency analysis with
877 historical information. *Journal of hydrology*, 313(1-2), 97-116.

878 SCHARDONG, A., SIMONOVIC, S. P., GAUR, A. & SANDINK, D. 2020. Web-Based Tool
879 for the Development of Intensity Duration Frequency Curves under Changing Climate at
880 Gauged and Ungauged Locations. *Water*, 12, 1243.

881 SCHIEMANN, R., LINIGER, M. & FREI, C. 2010. Reduced space optimal interpolation of
882 daily rain gauge precipitation in Switzerland. *Journal of Geophysical Research: Atmospheres*,
883 115.

884 ŞEN, Z. 2019. Annual Daily Maximum Rainfall-Based IDF Curve Derivation Methodology.
885 *Earth System Environment*, 3, 463–469. <https://doi.org/10.1007/s41748-019-00124-x>

886 SERRAT-CAPDEVILA, A., MERINO, M., VALDES, J. B. & DURCIK, M. 2016. Evaluation
887 of the performance of three satellite precipitation products over Africa. *Remote Sensing*, 8,
888 836.

889 SHAHID, S., POUR, S.H., WANG, X.-J. et al. 2017. Impacts and adaptation to climate change
890 in Malaysian real estate. *International Journal of Climate Change Strategies and Management*,
891 9(1), 87-103. <https://doi.org/10.1108/IJCCSM-01-2016-0001>

892 SHARIFI, E., EITZINGER, J. & DORIGO, W. 2019. Performance of the State-Of-The-Art
893 Gridded Precipitation Products over Mountainous Terrain: A Regional Study over Austria.
894 *Remote Sensing*, 11, 2018.

895 SHAWKY, M., MOUSSA, A., HASSAN, Q. K. & EL-SHEIMY, N. 2019. Performance
896 Assessment of Sub-Daily and Daily Precipitation Estimates Derived from GPM and GSMaP
897 Products over an Arid Environment. *Remote Sensing*, 11, 2840.

898 SOBRAL, B. S., DE OLIVEIRA-JÚNIOR, J. F., ALECRIM, F., GOIS, G., MUNIZ-JÚNIOR,
899 J. G., DE BODAS TERASSI, P. M., PEREIRA-JÚNIOR, E. R., LYRA, G. B. & ZERI, M.

900 2020. PERSIANN-CDR based characterization and trend analysis of annual rainfall in Rio De
901 Janeiro State, Brazil. *Atmospheric Research*, 238, 104873.

902 SOROOSHIAN, S., AGHAKOUCHAK, A., ARKIN, P., EYLANDER, J., FOUFOULA-
903 GEORGIOU, E., HARMON, R., HENDRICKX, J. M., IMAM, B., KULIGOWSKI, R. &
904 SKAHILL, B. 2011. Advancing the remote sensing of precipitation. *Bulletin of the American*
905 *Meteorological Society*, 92, 1271-1272.

906 SUN, Y., WENDI, D., KIM, D. E. & LIONG, S.-Y. 2019. Deriving intensity–duration–
907 frequency (IDF) curves using downscaled in situ rainfall assimilated with remote sensing data.
908 *Geoscience Letters*, 6, 17.

909 TAN, M. L. & DUAN, Z. 2017. Assessment of GPM and TRMM precipitation products over
910 Singapore. *Remote Sensing*, 9, 720.

911 TAN, M. L., IBRAHIM, A. L., DUAN, Z., CRACKNELL, A. P., CHAPLOT, V. (2015).
912 Evaluation of Six High-Resolution Satellite and Ground-Based Precipitation Products Over
913 Malaysia. *Remote Sensing*. 7: 1504-1528; Doi:10.3390/Rs70201504.

914 TAYLOR, K. E. 2001. Summarizing multiple aspects of model performance in a single
915 diagram. *Journal of Geophysical Research: Atmospheres*, 106, 7183-7192.

916 TIEN THANH, N. & DUTTO ALDO REMO, L. 2018. Projected changes of precipitation idf
917 curves for short duration under climate change in central Vietnam. *Hydrology*, 5, 33.

918 TRENBERTH, K. E. 2011. Changes in precipitation with climate change. *Climate Research*,
919 47, 123-138.

920 USHIO, T., SASASHIGE, K., KUBOTA, T., SHIGE, S., OKAMOTO, K. I., AONASHI, K.,
921 INOUE, T., TAKAHASHI, N., IGUCHI, T. & KACHI, M. 2009. A Kalman filter approach to
922 the Global Satellite Mapping of Precipitation (GSMaP) from combined passive microwave and
923 infrared radiometric data. *Journal of the Meteorological Society of Japan*. Ser. II, 87, 137-151.

924 WANG, X-J., ZHANG, J.-Y., SHAHID, S. et al. 2016. Adaptation to climate change impacts
925 on water demand. *Mitigation and Adaptation Strategies for Global Change*, 21(1), 81-99

926 WATT, E. & MARSALEK, J. 2013. Critical review of the evolution of the design storm event
927 concept. *Canadian Journal of Civil Engineering*, 40, 105-113.

928 WILLEMS, P. 2000. Compound intensity/duration/frequency-relationships of extreme
929 precipitation for two seasons and two storm types. *Journal of Hydrology*, 233, 189-205.

930 WRIGHT, D. B., SMITH, J. A., VILLARINI, G. & BAECK, M. L. 2013. Estimating the
931 frequency of extreme rainfall using weather radar and stochastic storm transposition. *Journal*
932 *of hydrology*, 488, 150-165.

933 YANG, P., XIA, J., ZHANG, Y., ZHAN, C. & QIAO, Y. 2018. Comprehensive assessment of
934 drought risk in the arid region of Northwest China based on the global palmer drought severity
935 index gridded data. *Science of the Total Environment*, 627, 951-962.

936 YANG, Y., WANG, G., WANG, L., YU, J. & XU, Z. 2014. Evaluation of Gridded
937 Precipitation Data for Driving SWAT Model in Area Upstream of Three Gorges Reservoir.

- 938 YAO, J., CHEN, Y., YU, X., ZHAO, Y., GUAN, X. & YANG, L. 2020. Evaluation of multiple
939 gridded precipitation datasets for the arid region of Northwestern China. *Atmospheric*
940 *Research*, 236, 104818.
- 941 YATAGAI, A., ARAKAWA, O., KAMIGUCHI, K., KAWAMOTO, H., NODZU, M. I. &
942 HAMADA, A. 2009. A 44-year daily gridded precipitation dataset for Asia based on a dense
943 network of rain gauges. *Sola*, 5, 137-140.
- 944 YUAN, F., ZHANG, L., SOE, K. M. W., REN, L., ZHAO, C., ZHU, Y., JIANG, S. & LIU, Y.
945 2019. Applications of TRMM-and GPM-era multiple-satellite precipitation products for flood
946 simulations at sub-daily scales in a sparsely gauged watershed in Myanmar. *Remote Sensing*,
947 11, 140.
- 948 YUE, S., & WANG, C. Y. (2004). A comparison of two bivariate extreme value distributions.
949 *Stochastic Environmental Research and Risk Assessment*, 18, 61-66.
- 950 ZAD, M., NAJJA, S., ZULKAFI, Z. & MUHARRAM, F. M. 2018. Satellite Rainfall (TRMM
951 3B42-V7) Performance Assessment and adjustment Over Pahang River Basin, Malaysia.
952 *Remote Sensing*, 10, 388
- 953 ZHU, B., CHEN, J., & CHEN, H. (2019). Performance of multiple probability distributions in
954 generating daily precipitation for the simulation of hydrological extremes. *Stochastic*
955 *Environmental Research and Risk Assessment*, 33(8-9), 1581-1592.
- 956 ZHU, D., YAO, H., JIANG, B. & YU, P. 2018. Negative log likelihood ratio loss for deep
957 neural network classification. arXiv preprint arXiv:1804.10690.